Research Square

Preprints are preliminary reports that have not undergone peer review.
They should not be considered conclusive, used to inform clinical practice,
or referenced by the media as validated information.

Interannual variability of regional daily precipitation extremes in subtropical Argentina: circulation features during early austral summer

Lorenzo Ricetti

lricetti@fcaglp.unlp.edu.ar

Universidad Nacional de La Plata Facultad de Ciencias Astronomicas y Geofisicas
https://orcid.org/0000-0001-8785-7020

Santiago Ignacio Hurtado
Fundacion Bariloche

Eduardo Andres Agosta
Universitat de Valencia

Lisandro Pinto
Universidad Nacional de La Plata Facultad de Ciencias Astronomicas y Geofisicas

Andres Cesanelli
Universidad Nacional de La Plata Facultad de Ciencias Astronomicas y Geofisicas

Research Article

Keywords: ENSO, SAM, extreme indices, teleconnections, trends, breakpoint

Posted Date: November 10th, 2026

DOI: https://doi.org/10.21203/rs.3.rs-11283277/v1

License: This work is licensed under a Creative Commons Attribution 4.0 International License.
Read Full License

Interannual variability of regional daily precipitation extremes in subtropical Argentina: circulation features during early austral summer

Lorenzo Ricetti [1,2,*] ORCiD: 0000-0001-8785-7020

Santiago I. Hurtado [1,2,3,4] ORCiD: 0000-0001-7843-0316

Eduardo A. Agosta [5,6] ORCiD: 0000-0003-1182-8877

Lisandro Pinto [1] ORCiD: 0009-0004-8568-6220

Andres Cesanelli [7] ORCiD: 0009-0006-9896-7499

[1] Climate, Variability and Extremes Research Group (CLAVE), Faculty of Astronomical and Geophysical Sciences, National University of La Plata (FCAG-UNLP), La Plata, Buenos Aires, Argentina.

[2] National Scientific and Technical Research Council (CONICET), Buenos Aires, Argentina.

[3] Fundación Bariloche, San Carlos de Bariloche, Río Negro R8400, Argentina.

[4] Fundación Patagonia AnalytiX, San Carlos de Bariloche, Río Negro R8400, Argentina.

[5] Department of Integral Ecology, Spanish Catholic Bishops' Conference, Madrid, Spain.

[6] Research group of climate change, weather risks and inputs to the hydrological system in the Mediterranean (CLIMAMET), University of Valencia, Valencia, Spain.

[7] Geophysical Research Center (CIGEOF), Faculty of Astronomical and Geophysical Sciences, National University of La Plata (FCAG-UNLP), La Plata, Buenos Aires, Argentina.

[(*)] Corresponding author lricetti@fcaglp.unlp.edu.ar

Abstract

Subtropical Argentina concentrates most of the country's population and economic activity, including rainfed agriculture in the La Plata Basin, where daily precipitation extremes drive flash flooding and crop losses. This study characterizes their interannual variability in early austral summer (November–January) through joint statistical and dynamical analysis. The R95p index was computed at rain gauges over 1961–2020, and a stepwise correlation-based regionalization grouped them into seven coherent regions spanning the full climatic gradient. Regional centroids were analysed for trends, breakpoints and periodicities, and used to composite ERA5 fields. Extreme precipitation increased over the north of the domain, as a significant linear trend in the northeast and as an abrupt 1984 breakpoint in the northwest. In every region, variability is organized by anomalous low-level moisture transport and convective instability, but moisture sources follow a longitudinal rule opposite to ocean proximity: eastern regions are fed by northerly transport along the eastern Andes, inland regions by easterly Atlantic inflow, except the northwest, which switched to the northerly pathway after 1984. Large-scale forcing follows the same partition: ENSO imprints a robust, linear signal over the Littoral and northeast, weakens along the semi-arid diagonal, and gives way to the Southern Annular Mode in the northwest, where the relationship reverses sign after 1984, shifting from a low-level mass-field pathway to jet-entrance ageostrophic ascent. Over coastal Buenos Aires, a significant Niño3.4 correlation is not supported by the circulation, showing that statistical association alone can mislead attribution.

Keywords ENSO, SAM, extreme indices, teleconnections, trends, breakpoint

1. Introduction

The sector of Argentine territory east of the Andes and north of 39° S (hereafter subtropical Argentina, STAr) encompasses the Pampas region, Cuyo, and the country's northeastern and northwestern extremes. It presents a heterogeneous topography (Fig. 1), set by the Andes, the central sierras, and the extensive subtropical plains, producing a pronounced zonal precipitation gradient and a wide range of climates, from arid conditions in the west to temperate and humid subtropical regimes in the east (Beck et al., 2018). The precipitation regime has a well-defined annual cycle, with a wet season concentrated between October and April and a dry season during austral winter (Barros et al., 2008; Sorensson & Ruscica, 2018). Wet-season accumulations account for roughly 85% of the annual total over the Pampas and Cuyo (Agosta and Compagnucci, 2012) and about 80% over northwestern Argentina (Ferrero and Villalba, 2019).

The eastern section of STAr overlaps with southeastern South America (SESA), a region widely referenced in the literature for the magnitude and persistence of its climate signals and for its hydrological relevance, as it contains a substantial fraction of the La Plata Basin. STAr concentrates most of Argentina's population and hosts economic activities that account for more than 80% of national gross domestic product, including rainfed agriculture, livestock production, and hydropower generation associated with the LPB (Bettolli et al., 2021; Maisonnave et al., 2026). At the same time, a significant fraction of the population is highly socially vulnerable, particularly in urban and peri-urban areas where poverty, informality, and infrastructure limitations amplify exposure to climate extremes (Lavell et al., 2012; Cardona, 2012). Daily precipitation extremes are therefore of particular concern, as they are directly associated with flash flooding, infrastructure damage, agricultural losses, and threats to public safety, with disproportionately severe impacts where adaptive and response capacities are limited (Handmer et al., 2012; Begum et al., 2022).

Given the relevance of these events, research on daily precipitation extremes in the region has focused mainly on characterizing long-term secular change to identify signals potentially attributable to anthropogenic forcing. At the regional scale, researchers have documented a sustained increase in extreme rainfall over SESA with high confidence (Seneviratne et al., 2021). This trend is consistent across station records (Haylock et al., 2006; Skansi et al., 2013; Olmo et al., 2020), gridded products (Castino et al., 2017; Ceron et al., 2021), reanalysis (Balmaceda-Huarte et al., 2021), and global climate models (Diaz et al., 2021), being SESA one of the South American regions with the largest rates of increase (Skansi et al., 2013). Beyond gradual trends, to the best of the authors' knowledge, only Ceron et al. (2021) have examined abrupt shifts or change points in extreme precipitation over the region. Regional projections point to a further intensification of the frequency and intensity of extremes under a range of emission scenarios, with broad agreement between dynamical (Blázquez and Solman, 2020; Reboita et al., 2022) and statistical downscaling approaches (Olmo et al., 2022). Models nonetheless show a wide spread in the magnitude, spatial pattern, and seasonality of the estimated trends. Over the historical period, this spread arises mainly from internal climate variability and structural inter-model uncertainty, whose relative contribution is largest at the regional scale and at interannual-to-decadal time scales (Hawkins and Sutton, 2009; Deser et al., 2012). Characterizing natural variability is therefore a prerequisite for interpreting both observed and projected trends

In contrast to trend studies, the analysis of abrupt shifts or change points in the mean of daily extreme precipitation indices remains scarce at the regional scale. To the best of the authors' knowledge, only Ceron et al. (2021) documented a change point in several indices of annual frequency of daily extreme precipitation over southern LPB, followed by an increase in the mean in the late 1990s. The authors attributed this shift to the abrupt change in subtropical Atlantic SST at the end of the twentieth century, linked to an anticyclonic circulation that enhanced moisture convergence over the region.

Given the scarcity of studies on abrupt shifts, the temporal variability of daily extremes and their associated forcings has also received comparatively little attention, although interest has grown over the past decades. At the interannual scale, El Niño-Southern Oscillation (ENSO) emerges as the leading modulator of daily precipitation extremes during the wet season. Grimm and Tedeschi (2009) identified a direct linear relationship between the Niño 3 index and the frequency of days exceeding the 90th percentile of precipitation over LPB from October to February, together with a nonlinear response in March–April. Consistently, Robledo et al. (2013) showed that the leading mode of covariability between an extreme precipitation intensity index (DIER75) and sea surface temperature (SST) during the wet season displays an ENSO-like pattern, with intensified extremes over central and eastern Argentina. More recently, Iacovone et al. (2024) reported consistent results for SESA during the October–December season, showing a direct, linear, and statistically significant relationship between the Oceanic Niño index and the accumulated precipitation in days above the 75th percentile. Conversely, Medina et al. (2025) found no robust or spatially coherent relationship between ENSO and the maximum one-day precipitation index (Rx1) over northwestern Argentina from December to March in the post-1970 period. Overall, the evidence points to a robust ENSO influence over the eastern portion of the region, while the relationship in the western portion has been only partially explored and appears more complex.

Beyond ENSO, other forcings have been linked to the interannual variability of regional precipitation extremes. Robledo et al. (2013) associated positive DIER75 anomalies over central and northern Argentina with warm anomalies in the tropical and subtropical Atlantic, while Robledo et al. (2016) and Iacovone et al. (2024) identified a significant Indian Ocean Dipole signal during September-November and during October–December, respectively. Regarding the Southern Annular Mode, Iacovone et al. (2024) reported significant negative correlations with SESA extremes in October–December, peaking in November. By contrast, Medina et al. (2025) found only spatially heterogeneous and isolated relationships for December–March with SAM.

Despite these advances, important limitations remain. First, the impact of the main climate forcings on daily extremes over the western portion of the study region has been explored only partially, and the available evidence is less consistent than in the east. Second, most of the studies mentioned above approach the problem from a predominantly statistical perspective, based on correlation analysis or on compositing indices across the phases of climate forcings. While such approaches identify significant relationships, their interpretation is limited, since statistical associations do not necessarily imply a causal link to the underlying dynamical processes. Robledo et al. (2016) and Medina et al. (2025) are exceptions, as they explicitly examine the anomalous tropospheric circulation associated with the extreme precipitation indices and address both the regional circulation and the large-scale patterns linked to different forcings. However, these studies analyze responses at individual stations and do not

assess them over coherent subregions. This is a relevant limitation for large-scale forcings, whose teleconnections are expected to be expressed over a region rather than at isolated points, where local responses can mask the signal.

Therefore, the aim of the present study is to characterize the interannual variability of daily precipitation extremes over coherent subregions of subtropical Argentina during early austral summer (November-January, NDJ). We also identify the climate forcings modulating this variability in each subregion, along with the regional-to-large-scale tropospheric circulation patterns that provide their dynamical underpinning. The choice of the NDJ season is not incidental. Most previous studies rely on the classical seasons, either austral spring (SON) or summer (DJF), whereas over the study region the highest thresholds of extreme precipitation within the wet season are reached in NDJ (Ricetti 2026). Additionally, November–January coincides with the window in which El Niño and La Niña events reach their maximum SST anomalies and regional influence (Anderson et al., 2017), which is key given that ENSO is the main interannual forcing in the region. We will address variability within the second half of the wet phase (February−April) separately in a forthcoming study.

The paper is organized as follows. Section 2 describes the data and methods used. Section 3 presents the results, covering the regionalization and the temporal behaviour of the regional series, their statistical links with the climate indices, and the associated tropospheric circulation. Section 4 discusses the results and Section 5 presents the conclusions.

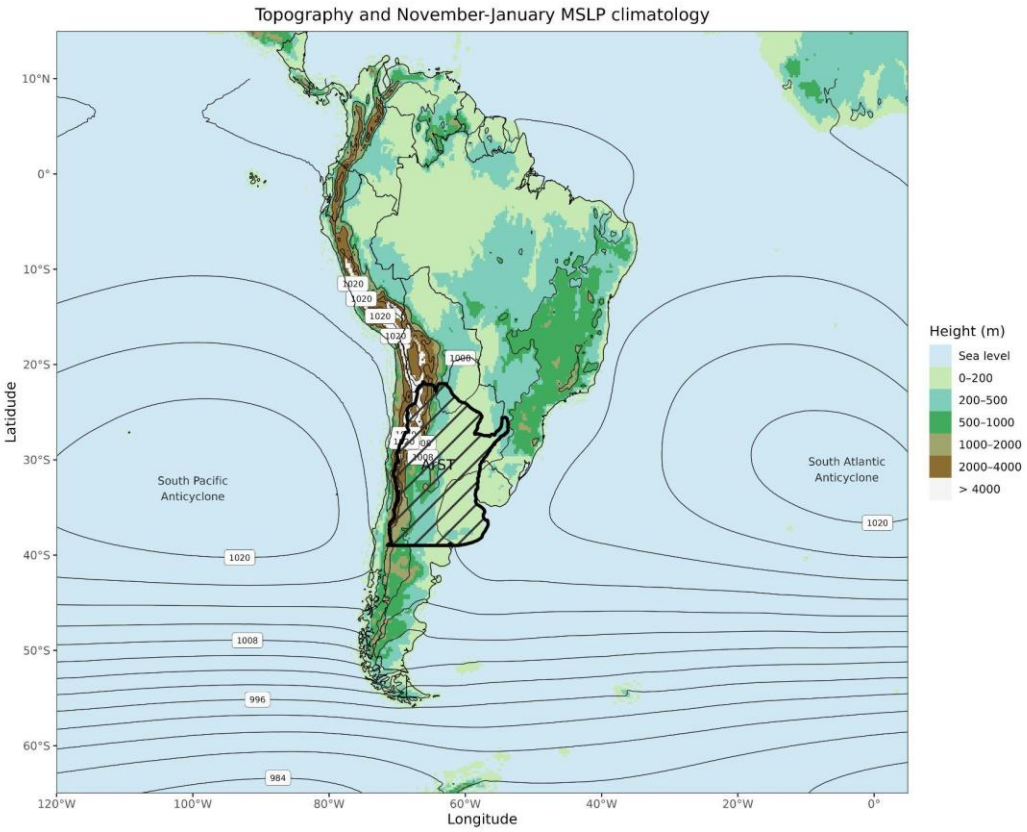


Figure 1. *ERA 5 South American topography (color shading) and November-January mean sea level pressure climatology (MSLP, black contours), showing the seasonal climatological position of the*

South Pacific and South Atlantic subtropical anticyclones. Base period: 1991-2020. The study region is shown in a hatched pattern.

2. Data and methods

2.1. Data

2.1.1. Station data

This study used daily accumulated precipitation records from the Argentine Meteorological Service (SMN). Although the records comply with World Meteorological Organization standards, we conducted a thorough quality-control analysis (see Ricetti et al., 2025a). Because this study focuses on wet extremes of precipitation, the quality-control procedure primarily targeted exceptionally large daily rainfall amounts, where potential inconsistencies could substantially influence the results. We evaluated suspect observations by comparing them with satellite data and measurements at surrounding stations. We also examined the atmospheric circulation associated with each case to determine whether the recorded precipitation was physically consistent with the prevailing synoptic conditions. After this analysis, we retained 62 rain gauges with less than 5% missing data within STAr (Figure 3A), spanning 1 Jan 1960–31 Dec 2021. We required stations with shorter records (17) to cover at least the minimum period considered (30 years; 1990–2021) to include them in the analysis.

In addition, monthly values of the observation-based Southern Annular Mode index (iSAM) within the study period were used (https://legacy.bas.ac.uk/met/gjma/sam.html, accessed 05 May 2026). This index is computed as the normalized difference in zonal-mean sea-level pressure between 40°S and 65°S, based on observations from 12 meteorological stations: six located at approximately 65°S and six at 40°S (Marshall, 2003).

2.1.2. Gridded products

For the analysis of ocean–atmosphere coupled system forcing, monthly sea surface temperature (SST) from the Extended Reconstructed Sea Surface Temperature version 6 (ERSSTv6) was used. Developed by the National Oceanic and Atmospheric Administration (NOAA), this dataset provides a global SST product at 2° × 2° resolution, spanning 1850–2025 (https://www.ncei.noaa.gov/products/extended-reconstructed-sst, accessed May 2026). ERSSTv6 is reconstructed primarily from in situ ship measurements, supplemented with observations from drifting buoys. Compared with its previous version, ERSSTv6 incorporates an interpolation method based on artificial neural networks, yielding improved spatial coherence and reduced root-mean-square error (Huang et al., 2025).

To analyze anomalous tropospheric circulation, we used monthly ERA5 fields (Hersbach et al., 2020; https://cds.climate.copernicus.eu/datasets, accessed February 2026). In particular, convective available potential energy (CAPE), mean sea level pressure (MSLP), geopotential height (GH) at 250 and 850 hPa, meridional and zonal wind at 250 and 850 hPa, vertically integrated moisture flux (VIMF) and its divergence. To evaluate anomalous divergence zones, we derived the velocity potential (CHI) at 250 hPa, representing the irrotational component of the flow.

2.1.3. Data preprocessing

Because the mean of a random variable can exhibit secular trends, computing anomalies relative to a fixed climatological mean may introduce systematic bias when such a trend is present, affecting the assessment of low-frequency variability (L'Heureux et al., 2013). For a monotonically increasing trend, for instance, negative anomalies would tend to concentrate early in the series and positive ones toward its end.

Many variables and indices used in this study exhibit long-term, statistically significant trends, namely tropical SST (Deser et al., 2010), iSAM (Fogt and Marshall, 2020), and tropospheric variables such as low-level moisture flux, GH and MSLP (Montini et al., 2019; Jones, 2019; Reboita et al., 2019; Gulev et al., 2021).

To avoid their influence on the estimated variability, we computed anomalies relative to a non-stationary basic state. At each time point, we estimated the basic state using Locally Estimated Scatterplot Smoothing (LOESS; Cleveland and Devlin, 1988) with a 30-year moving window, consistent with the typical length of reference climatologies (Barry and Chorley, 2009). We then obtained anomalies as the difference between each observed value and its corresponding LOESS estimate. In the absence of a secular trend, the basic state is constant and equal to the period mean, recovering the classical definition of anomalies. We did not compute precipitation anomalies using this approach, as we address their trends separately (Section 2.5).

2.2. Climate indices

To identify potential large-scale forcings associated with low-frequency variability in regional extreme precipitation, we selected a set of climate indices. These indices follow the ones assessed by the IPCC Sixth Assessment Report, Working Group I (Cassou et al., 2021), for the Southern Hemisphere: the Marshall SAM index (iSAM), two indices of Pacific Ocean variability (Niño1+2 and Niño3.4), two of the Indian Ocean (IOBW and DMI), and two of the Atlantic Ocean (AMM and AZM). We computed each oceanic index using ERSST v6 data in the standard domains defined by the IPCC (Fig. 2) and its anomalies, following section 2.1.3.

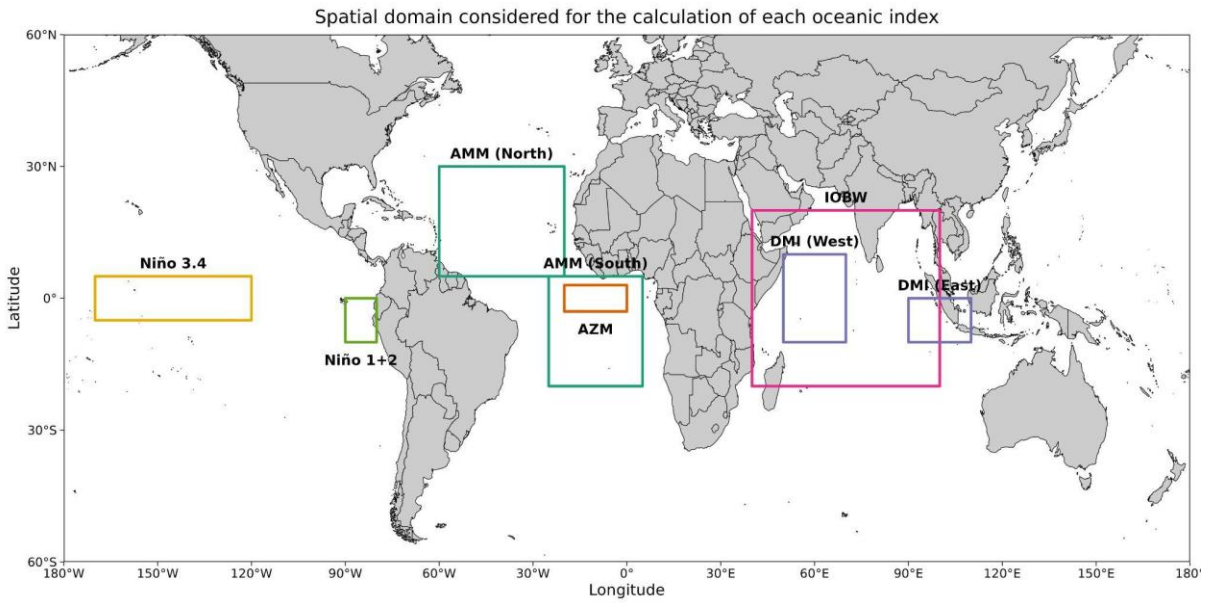


Figure 2*. Spatial standard domains over which the sea surface temperature anomalies at each grid point were area-averaged to obtain the considered indices, as defined by IPCC.*

2.3. Daily precipitation extreme index

To assess the spatio-temporal variability of daily precipitation extremes in STAr, the R95p index was used (Zhang et al., 2011). This interannual seasonal index was calculated at each of the 62 rain gauges within STAr as the rainfall sum on NDJ days exceeding the local daily 95th percentile. Each seasonal value was labeled by the year of its November–December months (i.e., the R95p value for 1981 comprises ND(1981) and J(1982)). The selection of this index was based on previous results (Ricetti et al., 2025a), which showed that R95p is the index that best synthesizes the spatio-temporal behavior of extreme precipitation in STAr, exhibiting the highest spatio-temporal coherence with frequency and intensity-based indices of extreme precipitation.

For regions with a marked annual cycle, such as STAr, using a single percentile for all days of the year is not recommended, since values exceeding it will naturally concentrate in the wettest months, as their probability of occurrence is not uniform throughout the annual cycle. Moreover, in these regions it is advisable to use the percentile of each calendar day, since the pronounced seasonality generates significant daily climatological differences, even within the same month, particularly during the austral spring (Grimm and Tedeschi, 2009).

The daily 95th empirical percentile for each rain gauge was estimated using the sample of all days (wet and dry), rather than a wet-day threshold sample. This choice follows the issue raised by Schär et al. (2016): estimating percentiles conditional on wet-day occurrence makes the resulting percentile sensitive to changes in the frequency of wet days, which can bias the identification of extreme events independently of any genuine change in rainfall intensity. Regarding the estimation scheme, percentiles were empirically-estimated using the sample 29-day moving window centered on the day to be estimated (Olmo and Bettolli, 2021), and the resulting estimated percentile annual cycle was smoothed with a Generalized Additive

Model (GAM). This estimation scheme showed the best overall performance in the percentile estimation-scheme benchmark by Ricetti et al. (2025b).

To ensure the statistical independence of the considered extreme events, a declustering procedure was applied (Tuel and Martius, 2021): consecutive days exceeding the threshold were treated as a single event, retaining only the day with the highest daily precipitation record. During index estimation, years with more than 10% missing daily data were excluded from the index calculation and set as missing. These missing values were interpolated using Multiple Linear Regression, with nearby stations as predictors selected via the Akaike Information Criterion (AIC). This imputation scheme has shown the best performance for hydro-meteorological series in the study region (Hurtado et al., 2021). Following this procedure, complete seasonal series of R95p were obtained for each of the 62 rain gauges, with one value per year for the entire study period.

2.4. Regionalization of daily precipitation extremes

We conducted a regionalization analysis to delimit homogeneous regions over which the R95p index shows temporally and spatially coherent behavior. In the literature, methods for regionalizing extreme precipitation fall into two categories: dimensionality reduction techniques (Santos et al., 2017; Akbas, 2023) and unsupervised machine learning algorithms (Sariş, 2020; Lima et al., 2021; Wang et al., 2021). In the study region, the most commonly used machine learning algorithms, k-means and Ward's method, were not able to deliver regions with simultaneous spatial and temporal coherence (Ricetti et al., 2025a). This limitation arises because these algorithms group all the available stations, whereas extreme precipitation in a complex-terrain domain such as STAr does not necessarily behave similarly among nearby stations, as it is strongly influenced by local features.

To avoid this problem and obtain spatio-temporally coherent regions, we used a stepwise correlation-based method developed by Hurtado et al. (2023). This algorithm (hereinafter HAZ method, after its authors' names) groups stations' time series based on the temporal co-variability of their series, allowing stations without a common signal to remain ungrouped rather than being forced into a region. Unlike k-means and Ward's method, HAZ does not require the number of regions to be specified in advance; instead, it requires two parameters: a critical correlation threshold (rc), defining the minimum acceptable correlation between each station's series and its group centroid, and a minimum number of stations required to form a region. In this study, rc = 0.6 was used, together with a minimum of four stations per region.

The algorithm operates on the standardized R95p index of each station, defined as its relative anomaly with respect to its temporal mean. The centroid of a set of selected stations is computed as their spatial average, and synthesizes the common interannual variability of the group. Starting from the full set of available stations, the algorithm iteratively

(i) removes the station with the lowest correlation to the centroid whenever this correlation falls below rc, and
(ii) incorporates the station with the highest correlation to the centroid whenever this correlation is equal to or greater than rc, recalculating the centroid after each step.

This procedure continues until neither condition applies; if the resulting set of stations meets the minimum required, it is retained as a region, and the process is repeated on the remaining stations until no further regions can be formed.

After the regions were defined, by construction the regional centroid has a correlation higher than 0.6 with the R95p index of every station that composes it. Consequently, the regional centroid of each region was considered to be representative of the temporal variability of extreme precipitation within that region.

2.5. Extreme precipitation trends and breakpoints

To evaluate linear trends in each regional centroid, we fitted a quantile regression to the median (τ = 0.5; Koenker and Bassett, 1978). Its slope (β) was tested using a two-tailed t-test (Wilks, 2011) under the null hypothesis of β = 0, with a 90% confidence level. Additionally, the presence of breakpoints or abrupt shifts in the time series was evaluated using the tests identified as best-performing by Hurtado et al. (2020): Pettitt (Pettitt, 1979), the Standard Normal Homogeneity Test (SNHT; Alexandersson, 1986), and Buishand Range (Buishand, 1982). Cerón et al. (2021) also applied these tests to daily extreme precipitation in the study region.

Given that the study period spans 60 years and that more than one breakpoint may occur, the multi-breakpoint scheme of the aforementioned tests, developed by Hurtado et al. (2020) was implemented. A maximum of two breakpoints per series was searched for, with a minimum subperiod length of 20 years. A breakpoint was considered valid when, for a given time series, at least two of the three tests identified a statistically significant break at a 90% confidence level within ±5 years of each other. For the SNHT test, surrogate time series were generated using 10,000 Monte Carlo simulations, while for Buishand-R, 10,000 bootstrap resamples of the series were used.

Given the interrelation between breakpoints and linear trends, a joint analysis of both was carried out. A significant breakpoint can spuriously produce a statistically significant monotonic trend when the full period is tested, without this reflecting a genuine, sustained increase or decrease of the variable (Ricetti et al., 2024; Cesanelli & Ricetti, 2025; Luo et al., 2026). Conversely, a genuine monotonic trend can spuriously lead to the detection of a breakpoint near the middle of the series. To disentangle these cases, the linear trend was additionally evaluated within each subperiod defined by the identified breakpoints. If the trend was significant over the full period but vanished within the subperiods, the inhomogeneity was attributed to the breakpoint and the full-period trend was considered spurious. Conversely, if the trend remained unchanged within the subperiods, the breakpoint was considered spurious and the inhomogeneity was attributed to the trend.

2.6. Variability and links with climate indices

We characterized the dominant periodicities of each regional centroid using wavelet spectral analysis (Torrence and Compo, 1998) with the Morlet wavelet ($\omega_0 = 6$). We compared the global wavelet power spectrum of each series with a null spectrum from 10,000 bootstrap resamples of the same series. We considered periods whose power exceeded the 90th percentile of this null distribution statistically significant.

To identify potential large-scale forcings associated with the low-frequency variability of the regional centroids, we computed the Pearson correlation coefficient between each centroid and each climate index described in Section 2.2. We assessed significance against the null hypothesis of zero correlation using a two-tailed test at a 90% confidence level.

2.7. Tropospheric circulation features

We applied a composite difference technique to tropospheric anomalies in years above the 75th percentile (high years) and below the 25th percentile (low years) in each region's series. We tested the difference between the high- and low-year composite anomalies using a two-tailed Welch's t-test at the 90% confidence level (Ruxton, 2006), under the null hypothesis that the difference is zero.

At the hemispheric scale, GH and Takaya-Nakamura wave activity flux (WAF; Takaya and Nakamura, 2001) at 250 hPa, together with the velocity potential, were composited to characterize the large-scale teleconnection pattern associated with each region's variability, as well as MSLP and the zonal component of wind at 250 hPa to assess the position of upper-level jets. At the regional scale, GH and wind at 850 hPa, VIMF and its divergence, and CAPE were composited to characterize the low-level circulation, moisture transport, and thermodynamic support linked to each region.

3. Results

3.1. Statistical analysis of regional time series: trends, breakpoints and variability

The HAZ method grouped 48 of the 62 rain gauges into seven spatio-temporally coherent regions (Fig. 3A). The remaining 14 stations did not share a common signal with any group, and the HAZ method left them ungrouped (crossed circles). Their spatial distribution is not random: most lie south of 30°S, and they align along the boundaries between regions, mainly where R1 meets R5, R7, R2 and R4, and along the R5–R7 limit, that is, in transition zones where no single regional signal prevails over the others. The seven regions span the full climatic gradient of subtropical Argentina, from the humid, forested northeast to the arid Andean foreland in the west.

R1 and R3 together make up the Argentine sector of SESA, the humid eastern half of the domain. R1 is the largest region (18 stations) and covers the Littoral and the northern Pampas, from southern Santa Fe and Entre Ríos to eastern Córdoba and northeastern Buenos Aires. It is a flat, humid plain drained by the Paraná and Uruguay rivers, whose floodplains and delta host extensive wetlands, and it concentrates the bulk of the country's rainfed grain and cattle production. To the north, R3 (6 stations) comprises northeastern Argentina: Misiones, eastern Chaco, Formosa and northern Corrientes. It is the wettest region of the study area and the

most heterogeneous in land cover, combining the Paranaense Atlantic forest on Misiones, the Iberá marshes, one of the largest wetland systems in South America, and the humid Chaco plain.

R6 comprises 5 stations across northwestern Argentina, from the Salta–Jujuy piedmont to western Formosa. It straddles a very sharp west–east rainfall gradient: the eastern Andean slopes sustain the Yungas subtropical montane cloud forest, while only a few hundred kilometers to the east the semi-arid Chaco begins. Despite these large contrasts in mean precipitation, the HAZ method groups these stations together because regionalization is based on the temporal coherence of the year-to-year variability rather than on the mean state.

Three regions lie along the semiarid diagonal, a belt of low precipitation that crosses South America from the Altiplano to Patagonia and is maintained by the rain shadow of the Andes. R5 (4 stations) corresponds to the La Rioja–Santiago del Estero lowlands, a hot, semi-arid dry-Chaco plain of thorn scrub; R7 (6 stations) to Cuyo (Mendoza and San Luis), an arid piedmont immediately east of the highest Andes, where agriculture is confined to snowmelt-fed irrigation; and R2 (4 stations), at the southeastern end of the diagonal, to southwestern Buenos Aires and eastern La Pampa, a sub-humid to semi-arid grassland plain interrupted by the low Ventania range. Finally, R4 (5 stations) occupies the southeastern corner of Buenos Aires province, facing the Atlantic. Being the region closest to the ocean, its precipitation is the most directly exposed to Atlantic conditions, and it is crossed from northwest to southeast by the Tandilia range.

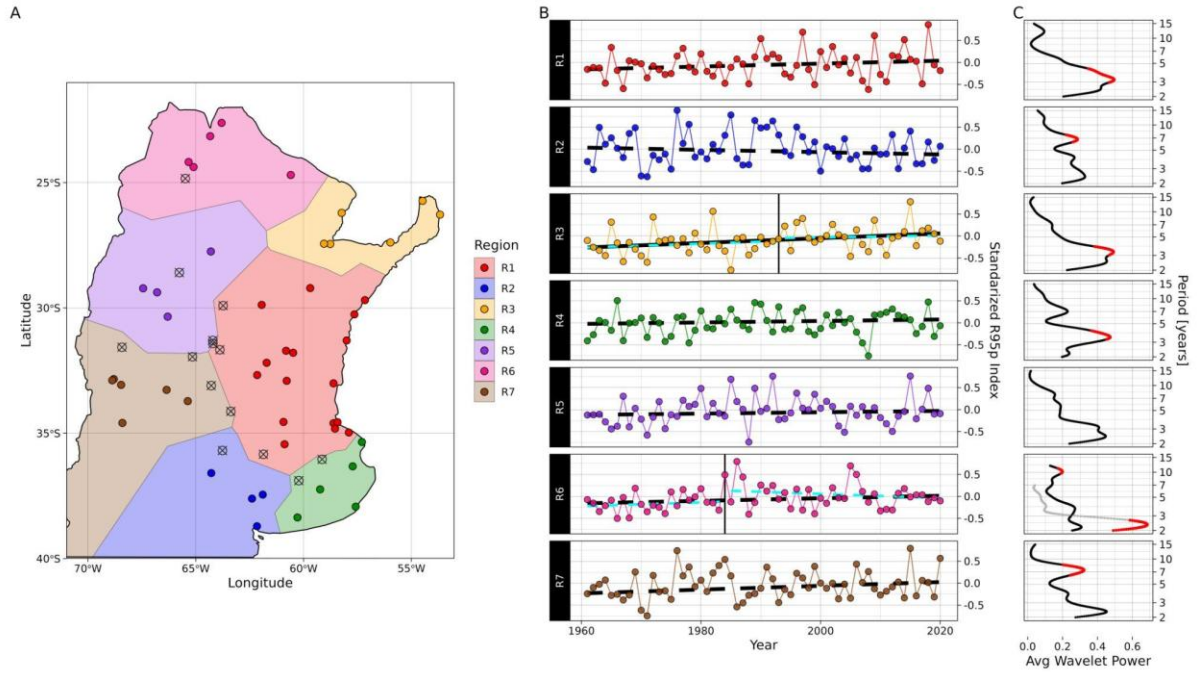


Figure 3. Panel A. *Rain gauge stations within the STAr domain, grouped by region, for which the November-December-January (NDJ) R95p index exhibited spatio-temporally coherent behavior (colored dots). Stations for which regionalization was not possible are marked with crossed circles. Thiessen polygons were constructed for the regionalized stations to delineate the spatial extent of each region (colored shade).* ***Panel B.*** *Standardized regional centroid time series of the NDJ R95p index,*

together with the corresponding linear trend of the centrality parameter (median regression). Trends with slopes significantly different from zero (two-tailed t-test, 90% confidence) are shown as solid lines; non-significant trends are shown as dashed lines. Black lines correspond to full-period trends, and cyan lines to trends within subperiods defined by breakpoints. Solid vertical lines mark the years of detected breakpoints according to the applied methodology. ***Panel C.*** *Global wavelet power spectrum of each regional time series. Power significantly exceeding the null spectrum at 90% confidence is shown in red. For the R3 time series, we removed the statistically significant trend before computing the spectrum. For R6, the power spectra before and after the 1984 breakpoint are shown in grey and black, respectively.*

Over the 1961–2020 period, all regional centroids except R2 exhibited increasing linear trends of the NDJ R95p index, although in R1, R4, R5, R6 and R7 the slopes were not significantly different from zero at the 90% confidence level, as was also the case for the decreasing trend of R2 (dashed lines in Fig. 3B). R3 was the only region with a statistically significant increasing trend over the full period.

Only three regions presented candidate breakpoints (Table 1). In R2, the three tests placed a shift toward lower values in 2000, but only Buishand-R was significant at a 90% confidence level. Since the adopted criterion requires agreement of at least two tests, the R2 time series was considered homogeneous. For R3, the three tests detected a significant shift toward higher values near the middle of the record, in 1990 for Pettitt and in 1993 for SNHT and Buishand-R. However, the linear trends computed within both subperiods remain increasing and comparable to that of the full period (Fig. 3B), so the inhomogeneity was attributed to the significant trend and the breakpoint was considered spurious (i.e., an artifact generated by the trend in the median). Conversely, in R6 the three tests agreed on a significant shift toward higher values in 1984 while trends within each subperiod showed opposing signs (slightly increasing before and decreasing after). Following the adopted methodology, we considered this shift a genuine breakpoint. The remaining regions were considered homogeneous over the study period, as none of the tests identified a statistically significant shift. Accordingly, we removed the significant trend in R3 before spectral analysis and subsequent analyses, and we analyzed R6 separately before (1961–1984) and after (1985–2020) its breakpoint.

Regarding the temporal variability, the global wavelet power spectra (Fig. 3C) reveal that the spectral band between 3 and 5 years dominates the eastern regions. R1 shows significant power between 3 and 5 years, peaking near 3 years; R4 in the 3-4.5-year band, and R3 in the 3–4-year band. Their similar spectral behavior is consistent with their geographical proximity within eastern STAr. Conversely, R2 and R7 concentrate their significant power in a lower-frequency band, between 6 and 9 years. Despite showing spectral peaks between 2.5-3.5 and 6-8 years, R5 was the only region whose global spectrum did not exceed the null spectrum at any periodicity. Lastly, R6's spectral behavior differed markedly between subperiods. Before the 1984 breakpoint, its significant power was concentrated in a high-frequency band of 2.5–3 years (Fig.3C, grey curve), whereas afterward the significant periodicities shifted to a decadal (9-12 years) band, with no significant power left at lower periods.

Table 1. *Breakpoint years identified in the regional centroid time series (rows), together with the p-values of the tests applied (columns). Bold shading indicates statistically significant breakpoints at 90% confidence, with upward/downward arrows indicating whether the break was toward higher or lower values.*

	Pettit	SNHT	Buishand-R
R1	1989 / 0.50	1989 / 0.19	1989 / 0.32
R2	2000 / 0.53	2000 / 0.17	**2000 / 0.085 (↓)**
R3	**1990 / 0.029 (↑)**	**1993 / 0.039 (↑)**	**1993 / 0.062 (↑)**
R4	1983 / 0.48	1983 / 0.31	1983 / 0.28
R5	1982 / 0.69	1982 / 0.43	1985 / 0.3
R6	**1984 / 0.075 (↑)**	**1984 / 0.037 (↑)**	**1984 / 0.062 (↑)**
R7	1996 / 1	1996 / 0.69	1996 / 0.68

3.2. Statistical links between large-scale forcing indices and regional extreme precipitation

The correlation analysis shows that interannual variability in the regional centroids in eastern STAr is essentially governed by Indo-Pacific forcing (Fig. 4), with most significant coefficients corresponding to the Pacific (Niño1+2, Niño3.4) and Indian Ocean (IOBW, DMI) indices. The Atlantic indices were almost unrelated to regional extreme precipitation over the domain as a whole: apart from a weak negative correlation between R3 and the AMM (−0.25), the only appreciable link was found in R6 before its breakpoint, where the AMM reaches a correlation of 0.46, a value that has no counterpart in the post-breakpoint period. The iSAM, in turn, was significant in only two regions: R5 and R6.

R1 and R3 showed the strongest links by far. In R3, the centroid correlates with IOBW (0.53), Niño1+2 (0.63), and Niño3.4 (0.67), the latter implying that ENSO linearly accounts for roughly 45% of the variance of regional extreme precipitation. R1 follows the same structure with somewhat lower values (0.39, 0.40 and 0.58, respectively), and is the only region where the DMI reaches statistical significance, though weakly (0.29). These correlations are consistent with the spectral behavior of both regions, whose significant power is concentrated in the characteristic ENSO band (3–5 years, Fig. 3C), and with their location in the Argentine sector of SESA, which is the part of STAr where the ENSO signal on precipitation is strongest.

Along the semi-arid diagonal, R2 and R7 also correlate significantly with El Niño and IOBW indices, but with markedly lower coefficients, close to 0.25 and a maximum of 0.37 for Niño3.4 and R2 centroid. This weaker coupling is consistent with their spectra, where significant power lies in the 6-8-year band rather than the classical ENSO band. R4, in contrast, represents the opposite situation: despite sharing with R1 and R3 significant power at higher frequencies, its only significant link is a weak correlation with Niño3.4 (0.23), suggesting that the interannual variability of extreme precipitation over the southeastern Buenos Aires coast is weakly related with the tropical Pacific.

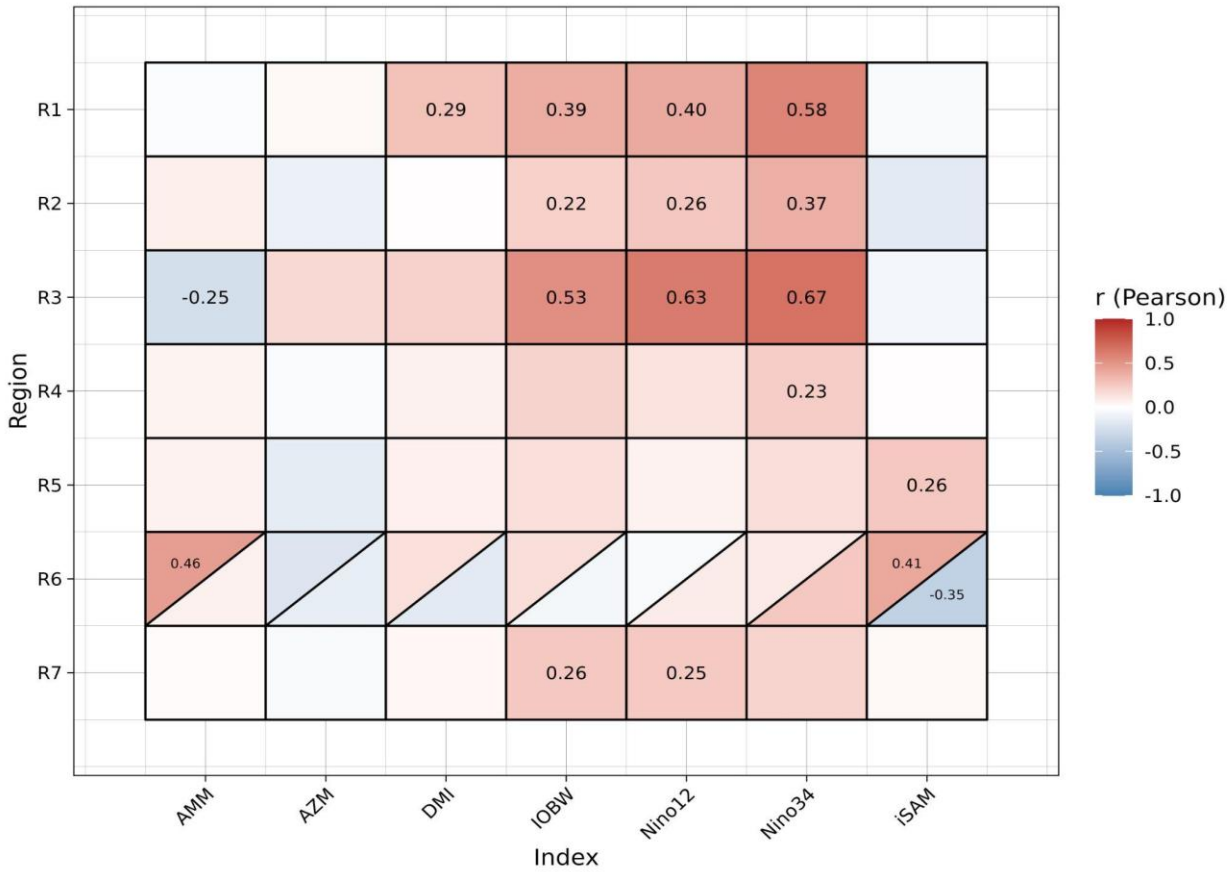


Figure 4. *Heatmap of Pearson correlation coefficients between the centroids of the different regions (y-axis) and the considered climate indices (x-axis) for the period 1961–2020. Coefficient values significantly different from zero (two-tailed test, 90% confidence) are shown as text. Cells corresponding to R6 are split into subsets before (upper) and after (below) the 1984 breakpoint.*

The two regions with no significant link to the Pacific or Indian Ocean indices, both located in northwestern STAr, are the only ones statistically related to the iSAM. R5, which showed no significant spectral peak at any period, correlates weakly but significantly with the iSAM (0.26). We evaluated R6 separately on either side of its breakpoint. Before the breakpoint, two coefficients were significant: the iSAM (0.41) and the AMM (0.46), while after the AMM link disappeared, the iSAM became the only significant coefficient with a negative sign (−0.35).

These results indicate that the breakpoint in R6 involved far more than a shift in the mean. The sign of the SAM–precipitation relationship reverses between the two subperiods, and the Atlantic link vanishes altogether, so the set of teleconnections modulating regional extreme precipitation seems different on either side of 1984. This is consistent with the complete reorganization of the power spectrum between the two subperiods (Fig. 3C), and together both lines of evidence point to a regime change rather than a simple shift in the mean level.

3.3. Tropospheric circulation features associated with interannual variability of regional extreme precipitation

Low-level composite differences of geopotential height and wind at 850 hPa show that some of the seven regions share similar lower-tropospheric circulation patterns associated with their variability (Fig. 5). In particular, R1, R3 and R6 after the breakpoint share their main

configuration: a positive, statistically significant GH anomaly over the subtropical lowlands of northeastern Argentina, Paraguay and southern Brazil, whose southwestern flank drives a significant anomalous northerly flow along the eastern side of the Andes towards the Littoral and northern Argentina (Fig. 5A, 5C and 5G). In R1, this anomaly is additionally accompanied by a significant negative GH center over southern South America and the adjacent Atlantic, which is weaker and non-significant in R3 and R6.

R1 and R3 also share several commonalities beyond this circulation pattern: they concentrate significant spectral power in the same 3–5-year band (Fig. 3C) and are the two regions most strongly correlated with the Pacific indices (Section 3.2). We therefore analyze them together in Section 3.3.1. In contrast, R6 lacks these additional commonalities, despite sharing the described regional circulation, and will therefore be examined separately.

R2 and R7 define a second group, characterized by a midlatitude GH dipole: an anticyclonic anomaly over the southwestern Atlantic centred near 50°S and a cyclonic anomaly over the southeastern Pacific, with the arid diagonal lying in between, under significant northeastern wind anomalies (Fig. 5B and 5H). The two centers are of comparable magnitude in R2 (differences near ±15 gpm), whereas in R7 the Atlantic anticyclone clearly dominates, exceeding 20 gpm. Consistently, both concentrate their significant power in the 6–9-year band and correlate only weakly with the Niño and IOBW indices, in contrast to the previous group.

A third group consists of R5 and pre-breakpoint R6. R5 exhibits a broad but weak anticyclonic anomaly over central-eastern Argentina and the adjacent Atlantic, barely reaching 10 gpm and with only limited areas of significant wind anomalies in its northwestern part (Fig. 5E). Pre-breakpoint R6 shows essentially the same structure (Fig. 5F): a positive geopotential height anomaly over the subtropical Atlantic whose northern flank drives an anomalous easterly flow onto the continent. This circulation is consistent with the only forcing they share with each other and with no other region: both are significantly and positively correlated with the iSAM, and neither is linked to the Pacific or Indian Ocean indices (Section 3.2). Accordingly, we analyze them together in Section 3.3.3. Moreover, it should be borne in mind that the pre-breakpoint R6 composite is built from only 12 seasons (6 high and 6 low), against the 30 (15 and 15) available for the remaining regions, so significance is harder to attain, and the weakly significant areas should not be read as absence of signal.

Lastly, in R4 the composite shows a negative GH anomaly over central and northern Argentina and a weak positive anomaly over the subtropical Atlantic, well to the east. R4 region lies between both centers, under significant anomalous northerly flow along the coast (Fig. 5D).

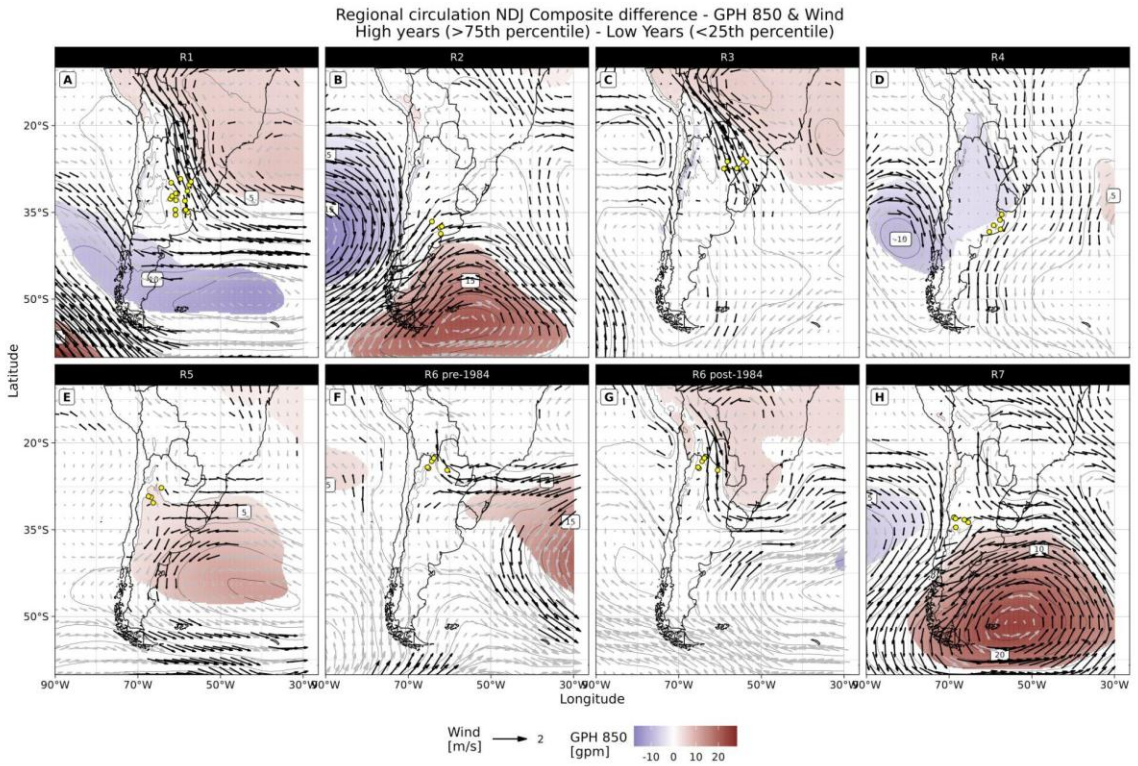


Figure 5. *November–January regional composite differences of geopotential height (GH, contours) and wind (vectors) at 850 hPa between years with high (>75th percentile) and low (<25th percentile) values of the regional centroid, for each region (panels). Shading and black vectors indicate differences significantly different from zero (Welch's t-test, two-tailed, 90% confidence); grey vectors are not significant. For R6, composites are shown separately for the periods before and after the 1984 breakpoint. Yellow dots in each panel mark the stations that make up the corresponding region.*

3.3.1. Regions R1 and R3 (Littoral and Northeastern Argentina)

The resemblance between R1 and R3 extends beyond the regional circulation (Fig. 5A and 5C) to the hemispheric scale, with both regions sharing the same SST composites and upper-level circulation. The description below is therefore based on R3, which shows the strongest links with the Pacific indices (Fig. 6), and the equivalent composite for R1 is given in Supplementary Fig. S1.

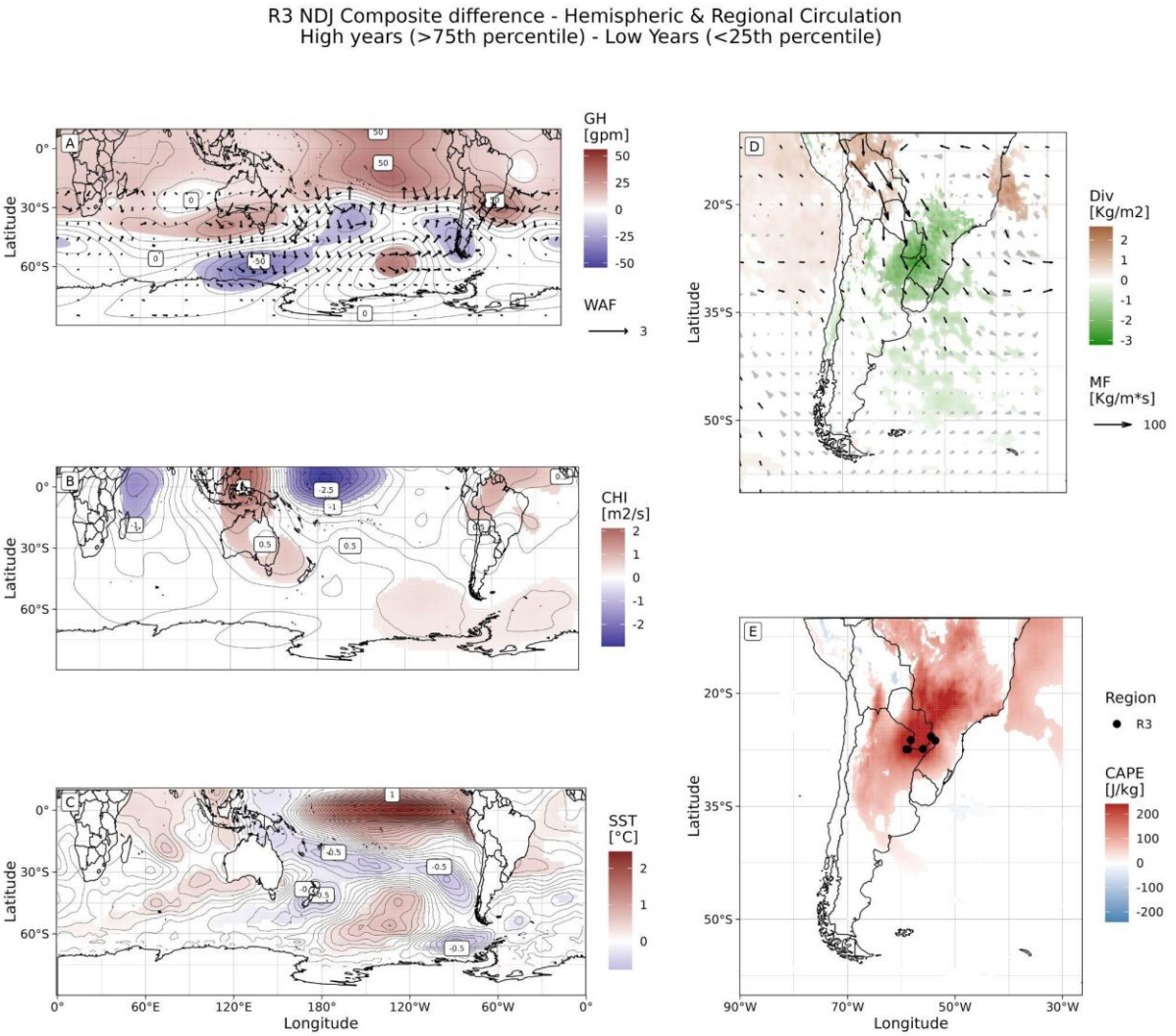


Figure 6. *November-January composite differences of anomalies between years with high (>75th percentile) and low (<25th percentile) values of the R3 centroid.* ***Left panels****: hemispheric composites of (A) geopotential height (GH, contours) and Takaya-Nakamura wave activity flux (WAF, vectors) at 250 hPa, (B) velocity potential (CHI) at 250 hPa, and (C) sea surface temperature (SST).* ***Right panels****: regional composites of (D) vertically integrated moisture flux (VIMF, vectors) and its divergence (shading), and (E) convective available potential energy (CAPE); location of R3 rain gauges are indicated in panel E with circles. Shaded values and black vectors indicate differences significantly different from zero (Welch's t-test, two-tailed, 90% confidence).*

The composite difference of SST anomalies shows the typical signature of El Niño, with positive statistically significant differences exceeding 2 °C along the central equatorial Pacific, flanked by negative anomalies over the western and subtropical South Pacific, and weaker though significant positive anomalies over the Indian Ocean basin (Fig. 6C), consistent with the correlation with climate indices. Consistently, the 250-hPa velocity potential shows significant upper-level divergence (negative CHI differences) over the central equatorial Pacific and western Indian Ocean basin and convergence over the Maritime Continent and northern Australia, as well as over northern South America (Fig. 6B), indicating an eastward displacement of the Walker circulation and anomalous upper-level convergence over the

Amazon. The GH composite difference at 250-hPa presents an arching quasi-stationary Rossby wave train in the extratropics, with alternating centres over the subtropical central Pacific, the Amundsen–Bellingshausen Seas, off central Chile, and over southern Brazil and the adjacent Atlantic (Fig. 6A). The WAF vectors indicate wave energy propagating from the subtropical western Pacific southeastwards and then northeastwards towards South America, in a structure resembling the Pacific–South American pattern associated with ENSO (Karoly, 1989; Mo and Nogués-Paegle, 2001).

At the regional scale, the anomalous northerly flow on the western flank of the low-level anticyclonic anomaly (Fig. 5C) is reflected in a significant southeastward moisture flux from the southern Amazon and the Bolivian lowlands along the eastern side of the Andes (Fig. 6D). This flux converges over southeastern Paraguay, northeastern Argentina, southern Brazil and Uruguay. Notably, moisture flux divergence is found over eastern Brazil, forming a dipole resembling the seesaw between the South Atlantic Convergence Zone and Southeastern South America (Nogués-Paegle and Mo, 1997). CAPE also increases significantly over the convergence area, with differences exceeding 200 J kg^{-1} over Paraguay, southern Brazil and northeastern Argentina (Fig. 6E). This evidence suggests that during years with high accumulated daily extreme precipitation in eastern STAr, enhanced low-level moisture transport towards the subtropical plains from lower latitudes, together with increased moisture convergence and convective instability, provides an environment favorable to extreme daily precipitation. This circulation is associated with a low-level anticyclonic anomaly as part of the hemispheric-scale circulation pattern typical of ENSO teleconnection.

3.3.2. Regions R2 and R7 (Argentine Semi-arid diagonal)

R2 and R7 variability is similar in every respect examined so far: their correlations with the climatic indices (Section 3.2), their common spectral peak near 7 years (Fig. 3C) and their regional circulation at 850 hPa (Fig. 5B and 5H). This similarity also extends to the SST and upper-level circulation composites. Therefore, the description below will be based on R2 (Fig. 7), and the equivalent composite for R7 is given in Supplementary Fig. S2.

The composite difference of geopotential height at 250 hPa displays a quasi-stationary wave train extending from the eastern subtropical Pacific towards South America and into the South Atlantic, with two significant negative centers reaching −45 gpm off the coast of central-southern Chile and a positive center exceeding 35 gpm over Patagonia and the southwestern Atlantic (Fig. 7A). This upper-level positive center lies above the anticyclonic anomaly at 850 hPa (Fig. 5B), indicating an equivalent barotropic structure. Consistently, the WAF vectors show Rossby wave energy emanating from the eastern tropical Pacific and propagating towards southern South America and further into the South Atlantic. The SST composite is consistent with this picture: significant positive differences exceeding 1.2 °C occupy the central equatorial Pacific and extend eastwards to the South American coast and then southwards along it (Fig. 7C), matching the relationship with the Niño1+2 and Niño3.4 indices described in Section 3.2. However, the WAF-identified wave source is not corroborated by the divergent circulation: the 250-hPa velocity potential shows no significant anomalies over the eastern equatorial Pacific (not shown). Instead, the zonal wind at 250 hPa does display a coherent, zonally elongated structure over the basin (Fig. 7B). Significant westerly anomalies extend across the central and eastern Pacific in both subtropical belts, averaging 3.5 m s^{-1} between

15°S and 25°S, and are separated by weaker easterly anomalies along the equator. This configuration is approximately symmetric about the equator and enhances the meridional shear of the zonal wind, linked to ENSO variations (Seager et al. 2005), and therefore the meridional gradient of absolute vorticity, on the flanks of both subtropical jets, a structure that can act as a Rossby wave source (Sardeshmukh and Hoskins, 1988).

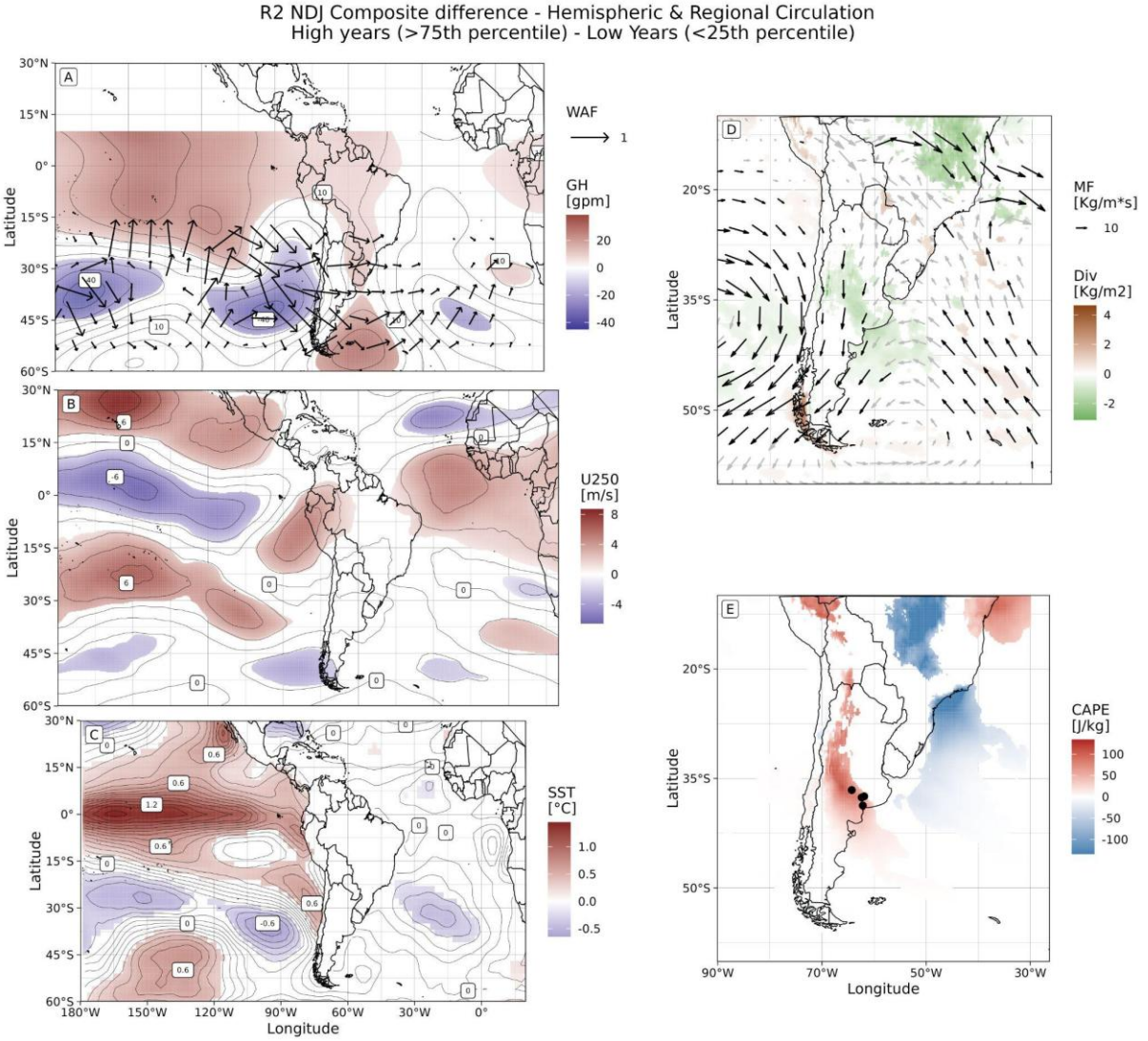


***Figure** 7. November-January composite differences of anomalies between years with high (>75th percentile) and low (<25th percentile) values of the R2 centroid. **Left panels**: composites of (A) geopotential height (GH, contours) and Takaya-Nakamura wave activity flux (WAF, vectors) at 250 hPa, (B) zonal wind at 250 hPa (U250), and (C) sea surface temperature (SST). **Right panels**: regional composites of (D) vertically integrated moisture flux (VIMF, vectors) and its divergence (shading), and (E) convective available potential energy (CAPE); the locations of R2 rain gauges are indicated in panel E with circles. Shaded values and black vectors indicate differences significantly different from zero (Welch's t-test, two-tailed, 90% confidence).*

At the regional scale, the anticyclonic anomaly over the southwestern Atlantic shown in Figure 5B is associated with an anomalous easterly to northeasterly moisture flux from the Atlantic

into central Argentina, between about 35°S and 40°S (Fig. 7D). This flux converges significantly over central-western Argentina, from the Andean foothills to the western Pampas, following Argentina's Arid Diagonal. CAPE also increases significantly over central-western Argentina between about 28°S and 45°S, covering the area where the stations of regions R2 and R7 are located (Fig. 7E). The two regions nevertheless differ in where their moisture comes from. Over R7, in the west, the inflow is predominantly easterly to northeasterly, entering the continent from the Atlantic at about 30°S to 35°S and crossing it westward towards the Andean piedmont (Fig. S2). To the east, the transport in R2 is instead mainly northerly, descending along the eastern side of the continent. The wave train that organizes both configurations is the same, and so is the thermodynamic response in CAPE; what changes between them is the pathway along which the moisture is delivered. This evidence suggests that seasons with high accumulated daily extreme precipitation within Argentina's Arid Diagonal are linked to enhanced static instability and moisture influx associated with an anticyclonic anomaly over the Patagonian coast as part of a short wave train emanating from the eastern Pacific basin.

3.3.3. Regions R5 and R6 pre-1984 breakpoint (northwestern Argentina)

R5 and pre-breakpoint R6, which already coincided in their regional circulation at 850 hPa (Fig. 5E and 5F) and in their positive correlation with the iSAM (Section 3.2), also share similar hemispheric features. The description below is based on R5 (Fig. 8), and the equivalent pre-breakpoint composite for R6 is shown in Supplementary Fig. S3.

The MSLP composite difference shows significant negative anomalies over Antarctica and the polar cap, poleward of 65°S, surrounded by a ring of weak positive anomalies at midlatitudes, significant mainly over the southern Indian Ocean and western Atlantic (Fig. 8A). Consistently, zonal wind shows significant westerly anomalies over subpolar latitudes (around 55–65°S) along most of the hemisphere, of about 2 m s^{-1} at 850 hPa, with significant easterly anomalies further equatorward over the Indian Ocean sector and west Atlantic (Fig. 8B). This annular structure, with lower pressure over the polar cap and westerlies displaced poleward, corresponds to the spatial pattern of the positive SAM phase (Thompson and Wallace, 2000), in agreement with the positive correlation found with iSAM in Section 3.2.

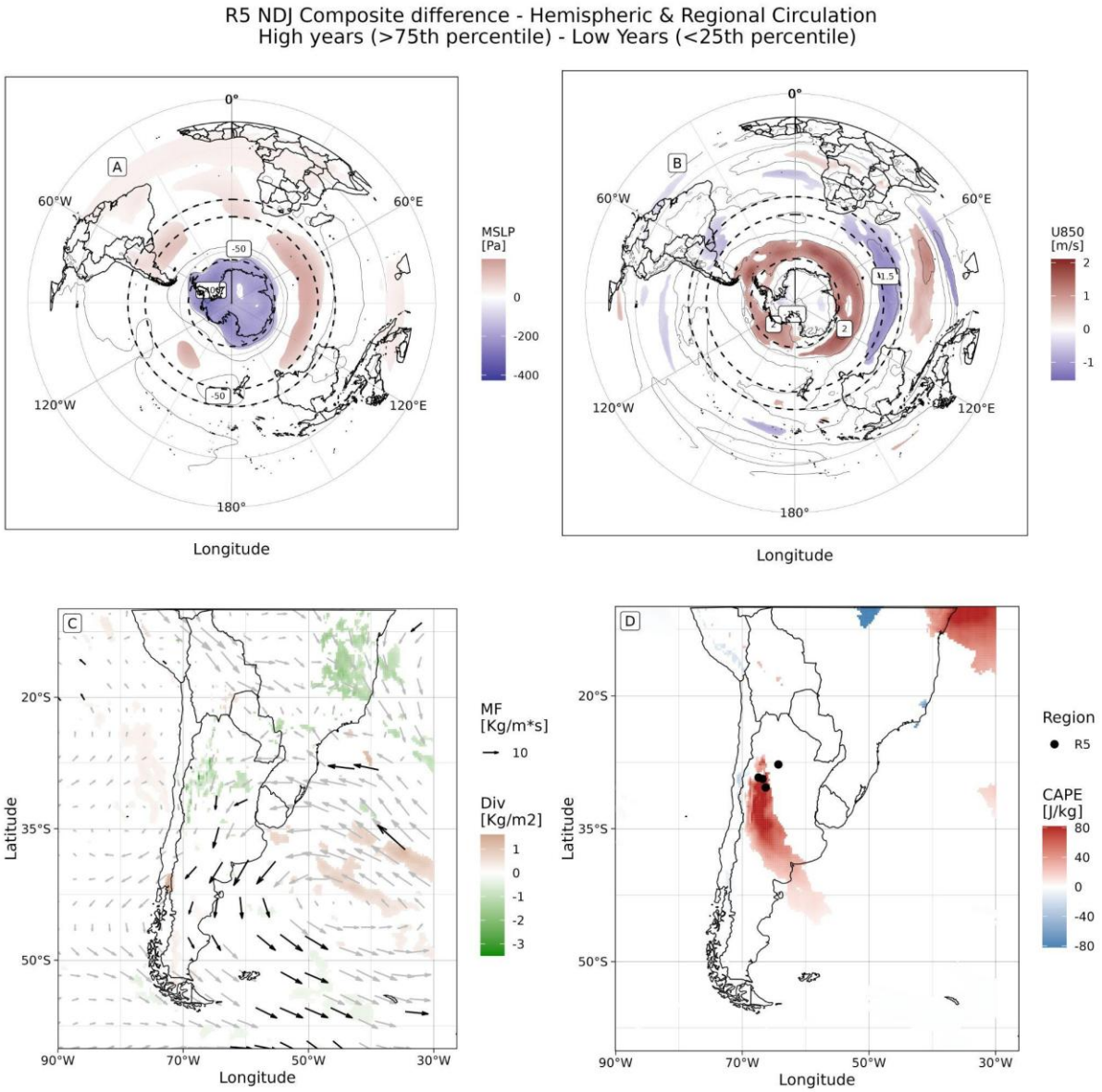


Figure 8. *November-January composite differences of anomalies between years with high (>75th percentile) and low (<25th percentile) values of the R5 centroid.* ***Upper panels****: hemispheric composites of (A) Mean Sea Level Pressure (MSLP, shading), and (B) zonal wind at 850 hPa (U850, shading).* ***Lower panels****: regional composites of (C) vertically integrated moisture flux (VIMF, vectors) and its divergence (shading), and (D) convective available potential energy (CAPE); locations of R5 rain gauges are indicated in panel D with circles. Shaded values and black vectors indicate differences significantly different from zero (Welch's t-test, two-tailed, 90% confidence).*

At the regional scale, the moisture flux anomalies near R5 are weak (~10 kg m^{-1} s^{-1}) but channelled from the east, indicating an anomalous inflow of Atlantic moisture into the continent that converges at the eastern foothills of the Andes, over the region itself (Fig. 8C). CAPE, in contrast, increases significantly over R5 and along those same foothills, reaching 80 J kg^{-1} (Fig. 8D), following a pattern very similar to that of the R2–R7 group (see Fig. 7E), aligned with the semiarid diagonal. In summary, during years with high extreme precipitation in the northwestern sector, the circulation is characterized by anomalous inflow of Atlantic moisture driven by an intensified South Atlantic Anticyclone and a southward shift relative to its

climatological position, whose northern flank imposes an easterly component over northwestern Argentina. This surface pressure rise is embedded in a hemispheric annular pattern consistent with a positive SAM phase, with low pressures over Antarctica and a southward-displaced jet.

3.3.4. Region R4 (Southeastern Buenos Aires)

At the hemispheric scale, the GH anomaly composite difference and WAF show an extratropical quasi-stationary Rossby wave train propagating downstream from the central Pacific towards South America and into the South Atlantic (Fig. 9A). The 250-hPa GH composite difference shows significant centers of about 20–25 gpm along this path: positive over the extratropical central Pacific and negative off the coast of central Chile. However, the WAF divergence shows no clear wave source.

The SST composite shows significant positive differences approaching 0.9 °C confined to the central equatorial Pacific (Fig. S4A), resembling a Central Pacific ENSO (Takahashi et al., 2011; Cai et al., 2020) and consistent with R4 being significantly correlated only with the Niño3.4 index. In agreement with these SST anomalies, the 250-hPa velocity potential shows significant upper-level divergence over the western equatorial Pacific (Fig. S4B). Neither field, however, translates into wave propagation from the tropics: the WAF vectors show no wave activity north of the midlatitudes, and the wave train in Fig. 9A remains confined to the extratropics. It also cannot be attributed to enhanced baroclinicity in the basic flow, since the Eady growth rate shows no significant increase along the wave-train path (Fig. S4C). The wave train associated with R4 thus has no single identifiable source: the tropical forcing suggested by the SST and velocity potential fields is not transmitted to the extratropics, and the pattern appears instead to result from a combination of sources rather than from one dominant region.

The regional composites show a well-defined low-level moisture pattern. A significant anomalous northerly moisture flux extends from northeastern Argentina over the Littoral and the adjacent Atlantic. Significant moisture flux convergence covers the Argentine Littoral, Uruguay and southern Brazil, and extends southwards over the eastern Pampas and the adjacent Atlantic down to about 42°S (Fig. 9B). In concordance, CAPE also increases significantly over northeastern Argentina and the R4 coastal strip, from where it extends southeastwards over the ocean (Fig. 9C). These features are consistent with the northerly flow channeled between the negative GH anomaly to the west and southwest of the region and the positive anomaly over the subtropical Atlantic (Fig. 5D).

In summary, seasonal extreme precipitation variability in R4 is associated with a channeled northerly flow that enhances moisture convergence and convective instability over the region. This flow is driven by the zonal GH gradient between the negative anomaly to the west and the positive anomaly over the subtropical Atlantic, which is part of an extratropical Rossby wave train that appears to draw on multiple sources, with no evident link to ENSO or any other homogeneous planetary forcing.

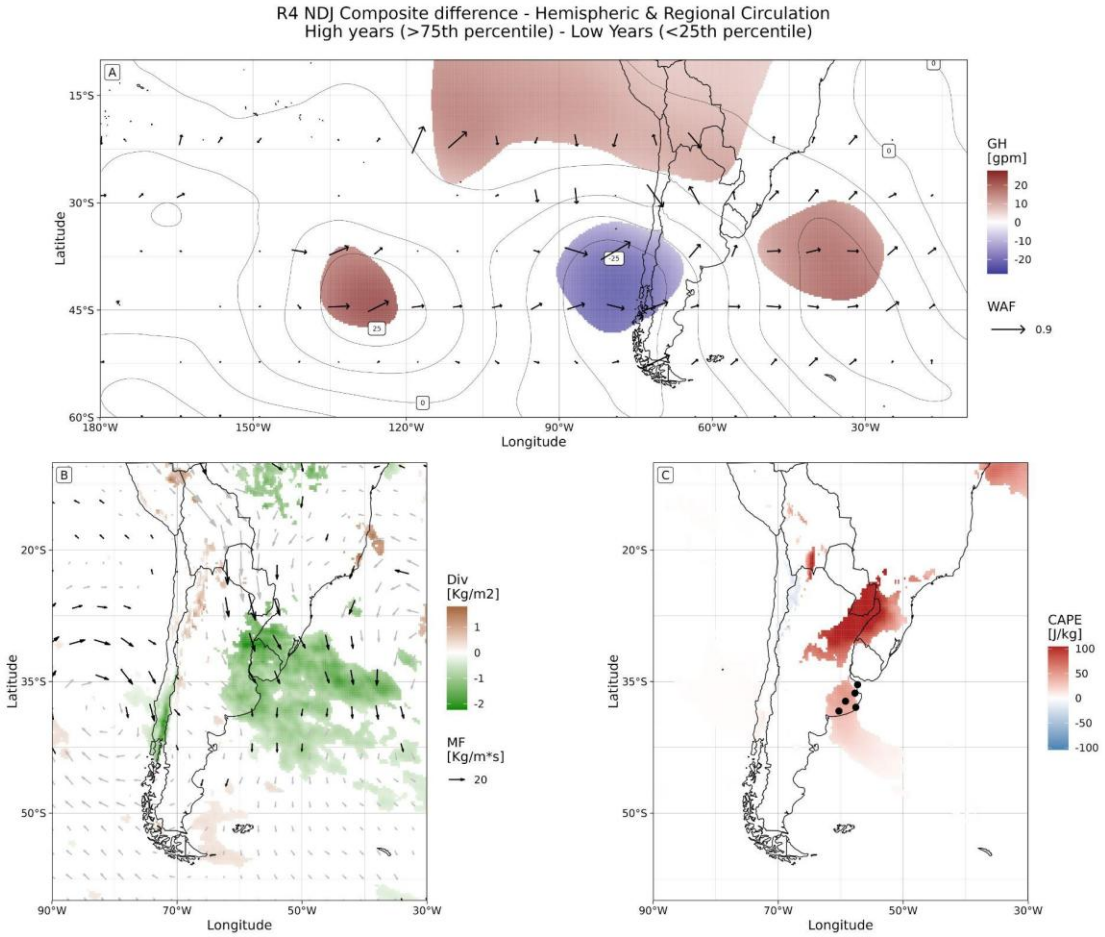


Figure 9. *November-January composite differences of anomalies between years with high (>75th percentile) and low (<25th percentile) values of the R4 centroid.* ***Upper panel****: (A) composites of geopotential height (GH, contours) and Takaya-Nakamura wave activity flux (WAF, vectors) at 250 hPa.* ***Lower panels****: regional composites of (B) vertically integrated moisture flux (VIMF, vectors) and its divergence (shading), and (C) convective available potential energy (CAPE); location of R4 rain gauges are indicated in panel C with circles. Shaded values and black vectors indicate differences significantly different from zero (Welch's t-test, two-tailed, 90% confidence).*

3.3.5. R6 post-1984 breakpoint (northwestern Argentina)

Unlike the previous cases, post-breakpoint R6 is not paired with any other region. Its low-level circulation reproduces the configuration of R1 and R3 (Fig. 5A, 5C and 5G), but it shares neither their spectral band (Fig. 3C) nor their teleconnections: it is the only region whose centroid correlates negatively with the iSAM, and it shows no significant link to the Pacific or Indian Ocean indices (Section 3.2). We therefore describe its composites separately (Fig. 10).

At the hemispheric scale, the zonal wind composite difference displays a well-defined annular structure of opposite sign to that of the previous group. At 850 hPa, significant easterly anomalies of about −1.5 m s^{-1} occupy subpolar latitudes between roughly 50°S and 65°S along most of the hemisphere, flanked by significant westerly anomalies of about 1.0–1.5 m s^{-1} throughout the midlatitude and subtropical belt, between about 20°S and 50°S (Fig. 10A). The same structure appears amplified at 250 hPa, with easterly anomalies reaching −3 m s^{-1} over the subpolar belt and westerly anomalies of about 4 m s^{-1} between 35°S and 50°S, together with significant easterly anomalies over the tropical belt (Fig. 10B). This configuration of weakened subpolar westerlies and a midlatitude jet displaced equatorward corresponds to the spatial pattern of the negative SAM phase (Thompson and Wallace, 2000), in agreement with the negative correlation with iSAM found for this subperiod in Section 3.2.

At the regional scale, the moisture flux anomalies are markedly stronger than in the pre-breakpoint composite and almost purely meridional: significant northerly transport of about 40 kg m^{-1} s^{-1} descends along the eastern side of the Andes into northwestern Argentina (Fig. 10C). This flux converges significantly over the region and its southern surroundings. Consistently, CAPE increases significantly over the same area, with differences exceeding 200 J kg^{-1} over the Salta–Jujuy piedmont (Fig. 10D).

In summary, after the 1984 breakpoint, seasons with high accumulated daily extreme precipitation at the extreme northwestern edge of STAr are associated with enhanced northerly moisture transport along the eastern Andes, which converges over the region and is accompanied by a marked increase in convective instability. This regional configuration is embedded in an annular hemispheric pattern corresponding to the negative SAM phase, with the midlatitude westerlies displaced equatorward. The mechanism therefore differs from the pre-breakpoint one not in the variables involved but in their sign and in the origin of the moisture: Atlantic easterly inflow under a positive SAM before 1984, northerly Andean transport under a negative SAM afterward.

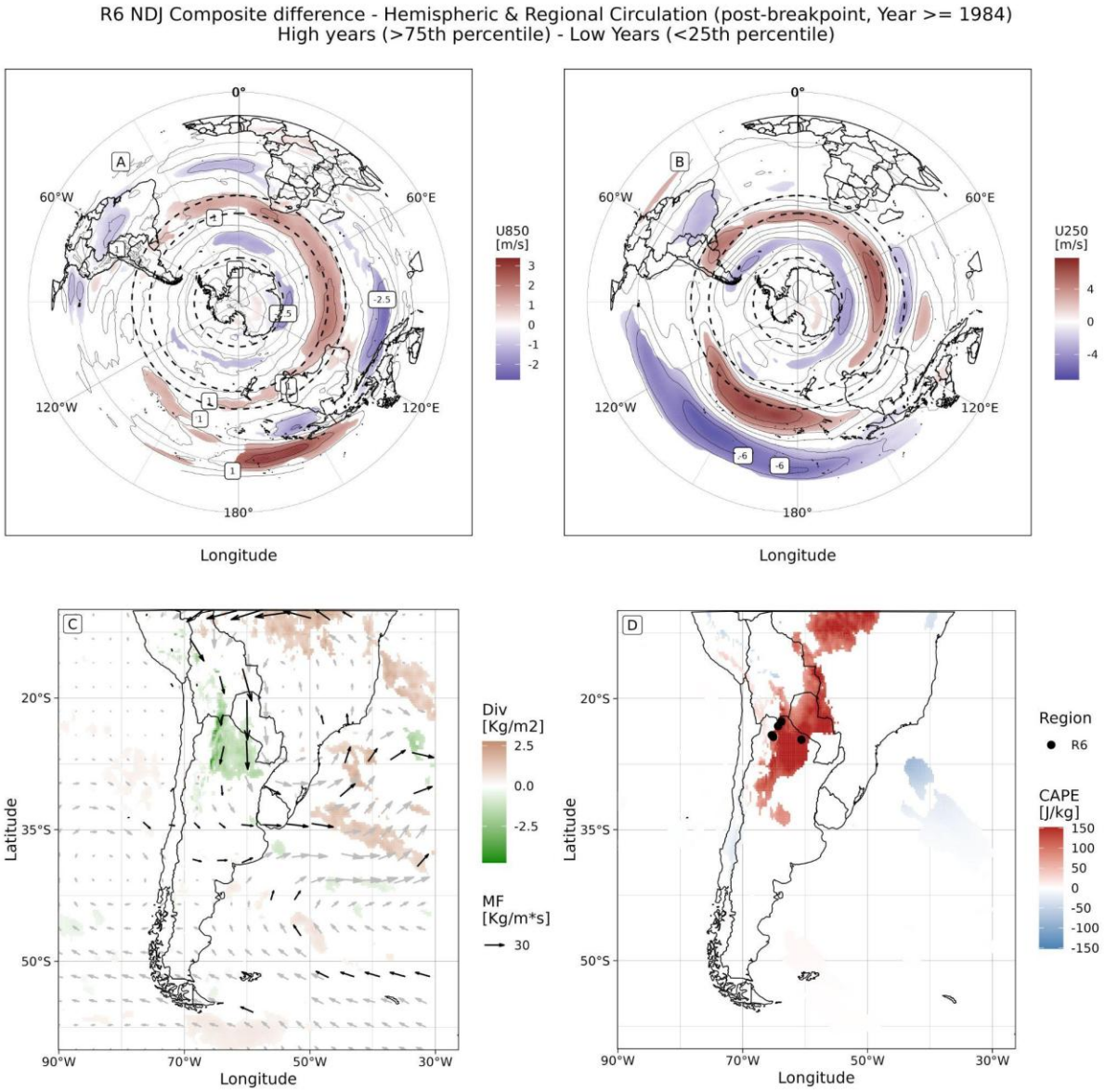


Figure 10. *November-January composite differences of anomalies between years with high (>75th percentile) and low (<25th percentile) values of the R6 centroid after the 1984 breakpoint.* ***Upper panels****: hemispheric composites of (A) zonal wind at 850 hPa (U850, shading) , and (B) zonal wind at 250 hPa (U250, shading).* ***Lower panels****: regional composites of (C) vertically integrated moisture flux (VIMF, vectors) and its divergence (shading), and (D) convective available potential energy (CAPE); locations of R6 rain gauges are indicated in panel D with circles. Shaded values and black vectors indicate differences significantly different from zero (Welch's t-test, two-tailed, 90% confidence).*

4. Discussion

In the northern part of the study region, a tendency towards larger extreme precipitation totals was identified in recent decades. In the northeast this appeared as a statistically significant increasing linear trend, whereas in the northwestern region it appeared as an abrupt breakpoint towards higher values in 1984. The increasing trends over the east are largely consistent with previous studies, although not unanimously. De Bodas Terrasi (2026) found no significant trends in extreme precipitation indices at stations near the Argentina–Brazil–Paraguay triple border over the same study period, possibly because different indices were used. In contrast, Balmaceda-Huarte et al. (2021) reported statistically significant trends in R95p over SESA during 1979–2017, both in station data and in some reanalyses. Similarly, Cerón et al. (2021) found significant increasing trends in the R10mm index from CHIRPS during summer over 1981–2018. To our knowledge, Cerón et al. (2021) is the only study that has assessed breakpoints in extreme precipitation indices within the study region. They identified a single breakpoint towards higher values over the southern La Plata Basin in 1999, but only in SON, with no breakpoints detected in austral summer. Although they applied the same tests as in the present study, they used a different index and did not include the western half of Argentina, which limits direct comparison.

The Littoral and northeastern regions, the wettest of the study area, carried a characteristic ENSO imprint at every stage of the analysis. Extreme precipitation variability in these regions was dominated by the 3–5 yr spectral band, within the characteristic ENSO band (Torrence & Webster, 1999), consistent with the power spectrum of the leading mode of co-variability between DIER75 and summer SST, which strongly imprints these regions (Robledo et al., 2013). They also showed the highest correlations with the ENSO indices, in agreement with the positive and significant correlations reported between the ONI and precipitation above the 75th percentile over SESA in the preceding season (October-December; Iacovone et al., 2024), and between Niño3.4 and Rx1day over northeastern Argentina during December–March (Medina et al., 2025). At the regional scale, their variability is modulated by a quasi-stationary anticyclonic anomaly centered in southern Brazil that brings northerly moisture advection and enhanced static instability, a configuration that agrees with the regional circulation and moisture transport reported by Robledo et al. (2016) for the leading mode in austral summer, and with the low-level circulations associated with ENSO described by Medina et al. (2025).

At the hemispheric scale, the regional anticyclonic anomaly is in turn part of a Rossby wave train characteristic of ENSO, forced by anomalous convection and upper-level divergence over the equatorial Pacific (Cai et al., 2020). Its structure combines the spring and summer patterns reported by Robledo et al. (2016) for extreme precipitation, as expected for the season analyzed here, and coincides with the El Niño configurations that produce the typical precipitation response over the region in November and December (Hurtado and Agosta, 2020). Overall, these regions exhibit a robust, linear and direct ENSO signal, consistent across every diagnostic and in agreement with the existing literature for this sector of SESA

Along the Argentine semi-arid diagonal, evidence for ENSO influence is considerably weaker and differs in kind, not just in degree. The Cuyo and dry Pampas regions concentrate their spectral power near 7 years, and their correlations with the Niño indices are statistically significant but low. This periodicity is consistent with the 6–8 yr band reported for precipitation during the wet phase over the western Pampas (Maenza et al., 2017). The SST composite shows significant anomalies over the central and eastern equatorial Pacific, but in a mixed

eastern–central configuration rather than the canonical pattern found in the eastern regions. This agrees with Tedeschi et al. (2015), who showed that the response of extreme precipitation over South America depends on the type of El Niño involved.

The circulation that modulates this variability is a short wave train whose positive center over Patagonia and the southwestern Atlantic drives anomalous easterly to northeasterly moisture inflow from the Atlantic into central Argentina, which converges along the arid diagonal and is accompanied by increased convective instability. Although the WAF indicates that the short wave train emanates from the eastern Pacific, the anomalous velocity potential shows a classical ENSO divergence pattern over the western part of the basin, away from the region where the wave originates. Therefore, the anomalous divergence associated with ENSO convection does not appear to drive the perturbation that governs regional variability.

Although the strongest ENSO signal over the Cuyo sector occurs in winter (Compagnucci and Vargas, 1998; Masiokas et al., 2006; Ricetti et al., 2025c), the weak summer relationship we find here is consistent with previous work on extreme precipitation. In particular, moisture flux divergence has been documented over the area occupied by R2 and R7 during central-Pacific La Niña events in DJF (Tedeschi et al., 2015), while Grimm & Tedeschi (2009) reported an increased frequency of extreme precipitation events over this region in November (Grimm and Tedeschi, 2009). In this sense, ENSO may act not through anomalous convection and divergence but through the configuration of the subtropical jets. The zonal wind composite shows significant westerly anomalies extending across the central and eastern Pacific in both subtropical belts, separated by easterly anomalies along the equator, in a configuration approximately symmetric about the equator (Seager et al., 2005). Such a symmetric strengthening and equatorward displacement of both subtropical jets is the expected extratropical signature of equatorially centered tropical heating (Seager et al., 2003, 2005), and by sharpening the meridional gradient of absolute vorticity, it makes the basic state more efficient at converting even a weak divergent outflow into a Rossby wave source (Sardeshmukh and Hoskins, 1988).

Beyond ENSO, the SAM modulates early-summer extreme precipitation variability over northwestern Argentina. The dry Chaco plains of La Rioja and Santiago del Estero, and the Andean piedmont of Salta and Jujuy before its 1984 breakpoint, are the only two regions showing no significant link to any Indo-Pacific index, and they are precisely the two that correlate positively with the iSAM. Set against the ENSO signal that dominates SESA at these same latitudes, this describes a longitudinal partition of the forcing across subtropical Argentina: tropical in the east, extratropical in the west. This positive relationship has precedents in the region. Iacovone et al. (2024) report positive and significant correlations between the SAM and precipitation above the 75th percentile over the extreme northwest of Argentina in December, and Cavalcanti et al. (2021) describe a dipolar structure in austral summer rainfall under SAM phases, with positive anomalies over northwestern Argentina during the SAM positive phase.

Consistent with these correlations, the composites show the annular structure of the positive SAM phase, with lower pressure over the polar cap and a poleward-displaced belt of westerlies, surrounded by a ring of positive pressure anomalies at midlatitudes (Thompson and Wallace, 2000; Fogt & Marshall, 2020). This ring projects onto the South Atlantic Anticyclone, intensifying it and shifting it south of its climatological position. Its northern flank

imposes an anomalous easterly flow that carries Atlantic moisture into the continent, converges at the eastern foothills of the Andes, and enhances convective instability over the region. Despite circulation similarities between the two northwestern regions, a caveat is in order. The pre-1984 breakpoint period spans only 23 seasons (1961–1983), so the composite difference for the northernmost region is built from 6 high and 6 low years, versus 15 and 15 for the other region, with no shift. This reduced sample lowers the test's statistical power (Wilks, 2011), so the lack of significance in parts of the domain should not be read as an absence of signal. Conversely, the areas that reach the 90% level despite that loss of power imply effect sizes large enough to emerge from a very small sample, supporting the pattern's robustness.

After 1984, the relationship between extreme precipitation over northwestern Argentina and the SAM reverses, changing from positive to negative, with both correlations statistically significant within their respective subperiods. The breakpoint is therefore not merely a year in which the series mean shifts abruptly, but one in which the structure of its variability also changes. Before 1984, the regional centroid's significant spectral power was confined to the 2–3 yr band, whereas afterward the only significant band was decadal, around 10 yr. The teleconnection itself therefore changed, both in sign and in the time scale on which it operates.

At the hemispheric scale, the composite is consistent with the negative phase of the SAM: higher pressure over the polar cap and midlatitude westerlies displaced equatorward. Over the South American sector this displacement produces significant easterly anomalies of about $-3.5\ \mathrm{m\ s^{-1}}$ poleward of 50°S and a positive zonal wind anomaly at 250 hPa centred near 36°S, that is, immediately poleward of the climatological axis of the subtropical jet, which in this longitude band lies at about 31°S and 200 hPa (Fig. 11). The region is thus located on the equatorward flank of the reinforced jet, and within its entrance region, since the climatological jet accelerates downstream towards the Atlantic. Consistently with the transverse ageostrophic circulation that develops at a jet entrance, whose ascending branch lies on the warm, equatorward side (Uccellini and Johnson, 1979; Keyser and Shapiro, 1986), the latitude–pressure cross-section averaged over the longitudes of the R6 rain gauges shows significant ascent between about 20°S and 27°S through the middle and upper troposphere, with subsidence poleward of 30°S and an ageostrophic meridional flow directed equatorward near the surface and poleward aloft. The region therefore lies beneath the ascending branch of the circulation forced by the jet anomaly, which supplies the dynamical lifting that accompanies the moisture convergence and the increased instability described above.

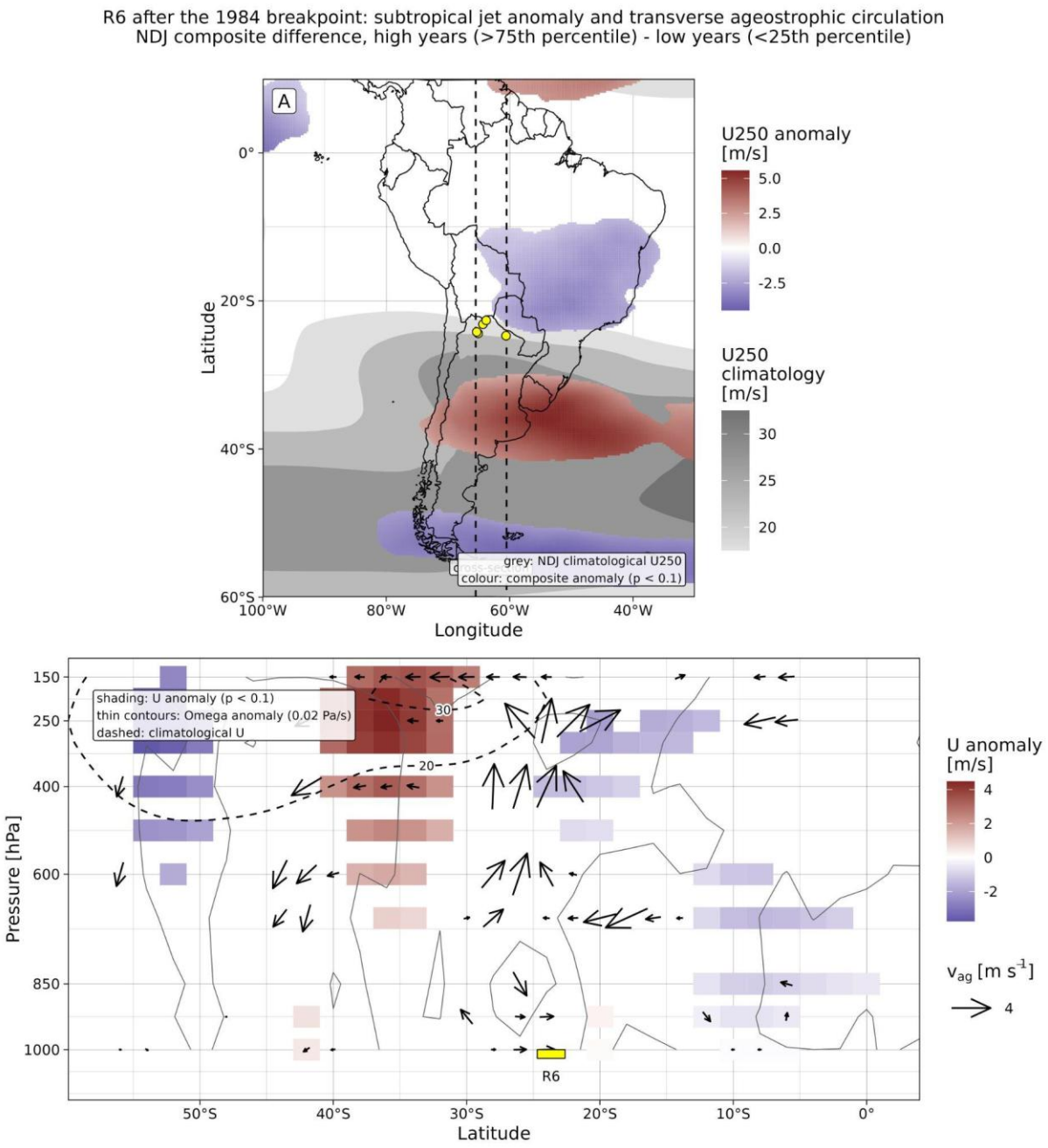


Figure 11. *November–January composite differences of anomalies between years with high (>75th percentile) and low (<25th percentile) values of the R6 centroid after the 1984 breakpoint.* ***Upper panel****: (A) zonal wind at 250 hPa (U250, colour shading) over the South American sector, superimposed on the NDJ climatology of U250 (grey shading; base period 1991–2020); the dashed box delimits the longitude band (65.5°W–60.5°W) over which the cross-section shown in the lower panel is averaged, and yellow dots mark the stations that make up R6.* ***Lower panel****: (B) latitude–pressure cross-section averaged over that band, showing the zonal wind anomaly (U, colour shading), the vertical velocity anomaly (ω, thin contours every 0.02 Pa s⁻¹) and the transverse ageostrophic circulation (vectors), the latter given by the meridional ageostrophic wind and −ω, with the vertical component scaled by 300 m s⁻¹ per Pa s⁻¹ and the reference arrow indicating the horizontal component. Dashed black contours show the climatological zonal wind (20 and 30 m s⁻¹) and the yellow bar on the abscissa marks the latitudinal range of the R6*

stations. Vectors are plotted only where more than half of the grid points within each 2° latitude bin are significant in either component. Colour-shaded values indicate differences significantly different from zero (Welch's t-test, two-tailed, 90% confidence).

Lastly, the coastal region of the Buenos Aires Province (R4) illustrates the limits of a mere statistical analysis. Its centroid correlates significantly with Niño3.4, and its SST and velocity potential composites display a coherent Central Pacific El Niño signature, with enhanced upper-level divergence over the western equatorial Pacific. Yet the wave train that organizes its regional circulation does not emanate there: the WAF shows wave activity equatorward from the midlatitudes crossing over southern South America, and the tropical signal does not propagate to the extratropics. Statistical association and dynamical causality therefore part ways in this case, arguing for examining the circulation itself rather than stopping at correlation with a climate index. At the regional scale, a northerly flow is organized between the negative geopotential height anomaly to the west and southwest of the region and the positive anomaly over the subtropical Atlantic. This flow transports moisture into the region, converges over it and over the adjacent ocean, and is accompanied by a significant increase in convective instability.

The comparison with the semi-arid diagonal is instructive. At essentially the same latitudes, regions farther inland draw moisture from the Atlantic through anomalous easterly inflow, whereas the coastal region of Buenos Aires, the one facing the ocean, is fed by a northerly flow of continental origin. Within this latitude belt the rule therefore runs opposite to what proximity to the ocean would suggest: the eastern regions are supplied by northerly transport along the eastern side of the Andes, and the western ones by easterly inflow from the Atlantic. Farther north, however, the partition is not geographical but temporal. The Andean piedmont of Salta and Jujuy follows the easterly, Atlantic pathway before 1984, as the dry Chaco plains do throughout the record, but after the breakpoint it switches to the northerly transport that characterizes the northeast. The regime change documented there therefore involves the moisture pathway itself, and not only the sign of the SAM relationship and the time scale on which it operates.

Both regions in which extreme precipitation increased are fed by this northerly pathway, the northeast throughout the record and the northwest after the 1984 breakpoint. These increases are consistent with the reported strengthening of the moisture transport by the South American low-level jet (SALLJ). Adduca et al. (2025) found significant increases in the annual and summer frequency of SALLJ days between 1979 and 2020, together with significant relationships between that frequency and precipitation anomalies over SESA, while Jones (2019) reported a substantial increase in the frequency and intensity of the jet along the eastern Andes over 1979–2017. Furthermore, Varuolo-Clarke et al. (2022) attributed between 20% and 45% of the observed austral summer precipitation trend over SESA to the increase in moisture flux carried by the jet. The increasing trend in the northeast and the post-1984 shift in the northwest are thus both consistent with a regime of more frequent and more intense northerly moisture transport in recent decades, although the present analysis does not evaluate that link directly.

5. Conclusions

This study characterizes the interannual variability of early austral summer (November-December-January) daily precipitation extremes over subtropical Argentina (STAr), going beyond the statistical diagnostics commonly relied upon in this type of work to examine the anomalous dynamics underlying that variability. Using a correlation-based regionalization method, STAr was partitioned into seven spatio-temporally coherent regions spanning the country's steep climatic gradient.

Our findings reveal a tendency towards larger extreme precipitation totals in the northern part of the domain over recent decades, manifested as an increasing linear trend over the northeast and as an abrupt breakpoint towards higher values in 1984 over the northwest. In every region the interannual variability is organized by anomalous low-level moisture transport, together with the convective instability anomalies that support these patterns, but the origin of that moisture follows a longitudinal rule opposite to what proximity to the ocean would suggest: the eastern regions are fed by northerly transport along the eastern side of the Andes, and the inland ones by easterly inflow from the Atlantic. The northwest is the exception, and a temporal rather than a geographical one, following the Atlantic pathway before 1984 and the northerly one afterwards. Both regions in which extreme precipitation increased are therefore supplied by that northerly transport, in line with the strengthening of the South American low-level jet reported in recent decades.

The large-scale forcing is partitioned along the same axis, with a tropical source in the east and extratropical in the west. ENSO imprints a robust, linear and direct signal over the Littoral and northeastern Argentina that weakens and changes in kind along the semi-arid diagonal, and gives way to the SAM over the northwest. That SAM relationship, however, is not stationary: it reverses sign at the 1984 breakpoint and the dominant time scale shifts from interannual to decadal. The reversal is not the mirror image of the earlier pattern, since the two phases act through different mechanisms: before the breakpoint through a low-level mass-field pathway, and afterwards through the transverse ageostrophic circulation that develops at the entrance of the reinforced subtropical jet, whose ascending branch supplies the dynamical lifting over the region. The teleconnection therefore changed not only in sign but in the process through which it operates, which a linear correlation over the full period would have masked.

The coastal region of the Buenos Aires Province shows that statistical relationships alone are not sufficient, and may lead to erroneous attributions when the circulation is not examined. Its centroid correlates significantly with Niño3.4 and its SST and velocity potential composites display a coherent Central Pacific El Niño signature, so that a purely statistical reading would have assigned its variability to ENSO. The wave train that actually organizes its regional circulation, however, does not emanate from the tropical Pacific but reaches the region from the midlatitudes. Statistical association and dynamical causality part ways in this case, and only the explicit examination of the circulation reveals it.

Ultimately, unraveling the dynamical mechanisms behind these subregional extreme events is a fundamental step toward improving subseasonal-to-seasonal predictability in southeastern South America, providing essential tools to mitigate the severe socio-economic impacts of flash flooding and agricultural losses in highly vulnerable areas.

Declaration of Competing Interest

The authors have no competing interest to declare.

CRediT authorship contribution statement

L. Ricetti: Conceptualization, Data curation, Formal analysis, Investigation, Methodology, Project administration, Software, Visualization, Writing - original draft. **S.I. Hurtado**: Conceptualization, Investigation, Methodology, Project administration, Supervision, Validation, Visualization, Writing - review & editing. **E.A. Agosta**: Investigation, Supervision, Validation, Writing–review & editing. **L. Pinto**: Investigation, Writing–review & editing. **A. Cesanelli**: Investigation, Writing–review & editing, Resources, Founding acquisition.

Funding

This work was supported by the National University of La Plata (UNLP), under grant PID-SG003 entitled “Caracterización de eventos extremos húmedos y secos en el sur de Sudamérica: forzantes asociados, cambios observados y proyectados y análisis de atribución”.

Declaration of generative AI in scientific writing

During the preparation of this work, the authors used Sonnet and Opus models from Claude AI in order to improve the wording and grammar of the manuscript. After using this tool/service, the authors reviewed and edited the content as needed and take full responsibility for the content of the publication.

References

Adduca, S., Hurtado, S. I., Zaninelli, P. G., & Aguirre Glik, J. O. (2025). Interannual variability of the South American low-level jet frequency and its impact on southeastern South America precipitation. Atmospheric Research, 326, 108331. https://doi.org/10.1016/j.atmosres.2025.108331

Agosta, E. A., & Compagnucci, R. H. (2012). Central-West Argentina summer precipitation variability and atmospheric teleconnections. Journal of Climate, 25(5), 1657-1677. https://doi.org/10.1175/JCLI-D-11-00206.1

Akbas, A. (2023). Seasonality, persistency, regionalization, and control mechanism of extreme rainfall over complex terrain. Theoretical and Applied Climatology, 152(3), 981-997. https://doi.org/10.1007/s00704-023-04440-1

Alexandersson, H. (1986). A homogeneity test applied to precipitation data. J. Climatol., 6: 661-675. https://doi.org/10.1002/joc.3370060607

Anderson, W., Seager, R., Baethgen, W., & Cane, M. (2017). Life cycles of agriculturally relevant ENSO teleconnections in North and South America. International Journal of Climatology, 37(8), 3297-3318. https://doi.org/10.1002/joc.4916

Balmaceda-Huarte, R., Olmo, M. E., Bettolli, M. L., & Poggi, M. M. (2021). Evaluation of multiple reanalyses in reproducing the spatio-temporal variability of temperature and precipitation indices over southern South America. International Journal of Climatology, 41(12), 5572-5595. https://doi.org/10.1002/joc.7142

Barros, V. R., Doyle, M. E., & Camilloni, I. A. (2008). Precipitation trends in southeastern South America: relationship with ENSO phases and with low-level circulation. Theoretical and Applied Climatology, 93(1), 19-33. https://doi.org/10.1007/s00704-007-0329-x

Barry, R. G., & Chorley, R. J. (2009). Atmosphere, weather and climate. Routledge.

Beck, H. E., Zimmermann, N. E., McVicar, T. R., Vergopolan, N., Berg, A., & Wood, E. F. (2018). Present and future Köppen-Geiger climate classification maps at 1-km resolution. Scientific Data, 5(1), 180214. https://doi.org/10.1038/sdata.2018.214

Begum, R., Lempert, R., Elham, A., Benjaminsen, T. A., Bernauer, T., Cramer, W., ... & Wester, P. (2022). Point of departure and key concepts. https://doi.org/10.1017/9781009325844.003

Bettolli, M. L., Solman, S. A., Da Rocha, R. P., Llopart, M., Gutierrez, J. M., Fernández, J., ... & Cuadra, S. V. (2021). The CORDEX Flagship Pilot Study in southeastern South America: a comparative study of statistical and dynamical downscaling models in simulating daily extreme precipitation events. Climate Dynamics, 56(5), 1589-1608. https://doi.org/10.1007/s00382-020-05549-z

Blázquez, J., Silvina, A.S. Multiscale precipitation variability and extremes over South America: analysis of future changes from a set of CORDEX regional climate model simulations. Clim Dyn 55, 2089–2106 (2020). https://doi.org/10.1007/s00382-020-05370-8

Buishand, T. A. (1982). Some methods for testing the homogeneity of rainfall records. Journal of hydrology, 58(1-2), 11-27. https://doi.org/10.1016/0022-1694(82)90066-X

Cai, W., McPhaden, M. J., Grimm, A. M., Rodrigues, R. R., Taschetto, A. S., Garreaud, R. D., ... & Vera, C. (2020). Climate impacts of the El Niño-southern oscillation on South America. Nature Reviews Earth & Environment, 1(4), 215-231. https://doi.org/10.1038/s43017-020-0040-3

Cardona, O.-D., van Aalst, M. K., Birkmann, J., et al. (2012). Determinants of Risk: Exposure and Vulnerability. In C. B. Field et al. (Eds.), Managing the Risks of Extreme Events and Disasters to Advance Climate Change Adaptation: Special Report of the IPCC (pp. 65-108). Cambridge University Press. https://doi.org/10.1017/CBO9781139177245.005

Castino, F., Bookhagen, B., & Strecker, M. R. (2017). Rainfall variability and trends of the past six decades (1950-2014) in the subtropical NW Argentine Andes. Climate Dynamics, 48(3), 1049-1067. https://doi.org/10.1007/s00382-016-3127-2

Cavalcanti, I. F. A., Barreto, N. J. C., Alvarez, M. S., Osman, M., & Coelho, C. A. S. (2021). Teleconnection patterns in the Southern Hemisphere represented by ECMWF and NCEP S2S project models and influences on South America precipitation. Meteorological Applications, 28(4), e2011. https://doi.org/10.1002/met.2011

Cerón, W. L., Kayano, M. T., Andreoli, R. V., Avila-Diaz, A., Ayes, I., Freitas, E. D., ... & Souza, R. A. (2021). Recent intensification of extreme precipitation events in the La Plata Basin in Southern South America (1981-2018). Atmospheric Research, 249, 105299. https://doi.org/10.1016/j.atmosres.2020.105299

Cesanelli, A., & Ricetti, L. (2025). Análisis exploratorio de la variabilidad en baja frecuencia de la precipitación anual y estacional en La Plata Observatorio. Geoacta, 46. http://sedici.unlp.edu.ar/handle/10915/176370

Cleveland, W. S., & Devlin, S. J. (1988). Locally Weighted Regression: An Approach to Regression Analysis by Local Fitting. Journal of the American Statistical Association, 83(403), 596–610. https://doi.org/10.1080/01621459.1988.10478639

Compagnucci, R.H. and Vargas, W.M. (1998), Inter-annual variability of the Cuyo rivers' streamflow in the Argentinean Andean mountains and ENSO events. Int. J. Climatol., 18: 1593-1609. https://doi.org/10.1002/(SICI)1097-0088(19981130)18:14<1593::AID-JOC327>3.0.CO;2-U

Deser, C., Phillips, A., Bourdette, V., & Teng, H. (2012). Uncertainty in climate change projections: the role of internal variability. Climate Dynamics, 38(3), 527-546. https://doi.org/10.1007/s00382-010-0977-x

Díaz, L. B., Saurral, R. I., & Vera, C. S. (2021). Assessment of South America summer rainfall climatology and trends in a set of global climate models large ensembles. International Journal of Climatology, 41, E59-E77. https://doi.org/10.1002/joc.6643

Ferrero, M. E., & Villalba, R. (2019). Interannual and long-term precipitation variability along the subtropical mountains and adjacent Chaco (22-29°S) in Argentina. Frontiers in Earth Science, 7, 148. https://doi.org/10.3389/feart.2019.00148

Fogt RL, Marshall GJ. The Southern Annular Mode: Variability, trends, and climate impacts across the Southern Hemisphere. WIREs Clim Change. 2020; 11:e652. https://doi.org/10.1002/wcc.652

Grimm, A. M., & Tedeschi, R. G. (2009). ENSO and extreme rainfall events in South America. Journal of Climate, 22(7), 1589-1609. https://doi.org/10.1175/2008JCLI2429.1

Gulev, S. K., Thorne, P. W., Ahn, J., Dentener, F. J., Domingues, C. M., Gerland, S., ... & Hawkins, E. (2021). Changing state of the climate system. Climate change 2021: The physical science basis. Contribution of working group I to the sixth assessment report of the intergovernmental panel on climate change, 287-422. https://doi.org/10.1017/9781009157896.004

Handmer, J., Honda, Y., Kundzewicz, Z. W., Arnell, N., Benito, G., Hatfield, J., ... & Yamano, H. (2012). Changes in impacts of climate extremes: human systems and ecosystems. In Managing the Risks of Extreme Events and Disasters to Advance Climate Change Adaptation: Special Report of the IPCC (pp. 231-290). https://doi.org/10.1017/CBO9781139177245.007

Hawkins, E., & Sutton, R. (2009). The potential to narrow uncertainty in regional climate predictions. Bulletin of the American Meteorological Society, 90(8), 1095-1108. https://doi.org/10.1175/2009BAMS2607.1

Haylock, M. R., Peterson, T. C., Alves, L. M., Ambrizzi, T., Anunciação, Y. M. T., Báez, J., ... & Vincent, L. A. (2006). Trends in total and extreme South American rainfall in 1960-2000 and links with sea surface temperature. Journal of Climate, 19(8), 1490-1512. https://doi.org/10.1175/JCLI3695.1

Hersbach H, Bell B, Berrisford P, et al. The ERA5 global reanalysis. Q J R Meteorol Soc. 2020; 146: 1999–2049. https://doi.org/10.1002/qj.3803

Huang, B., Yin, X., Boyer, T., Liu, C., Menne, M., Rao, Y. D., ... & Zhang, H. M. (2025). Extended Reconstructed Sea Surface Temperature, version 6 (ERSSTv6). Part II: Upgrades on quality control and large-scale filter. Journal of Climate, 38(4), 1123-1136. https://doi.org/10.1175/JCLI-D-24-0185.1

Hurtado, S. I., Zaninelli, P. G., & Agosta, E. A. (2020). A multi-breakpoint methodology to detect changes in climatic time series. An application to wet season precipitation in subtropical Argentina. Atmospheric Research, 241, 104955. https://doi.org/10.1016/j.atmosres.2020.104955

Hurtado, S. I., Zaninelli, P. G., Agosta, E. A., & Ricetti, L. (2021). Infilling methods for monthly precipitation records with poor station network density in Subtropical Argentina. Atmospheric Research, 254, 105482. https://doi.org/10.1016/j.atmosres.2021.105482

Hurtado, S. I., Agosta, E. A., & Zaninelli, P. G. (2023a). Monthly variations of forcing mechanisms of austral summer precipitation in subtropical Argentina. Atmospheric Research, 285, 106609. https://doi.org/10.1016/j.atmosres.2023.106609

Iacovone, M. F., Pántano, V. C., & Penalba, O. C. (2024). The relationship between ENSO, IOD and SAM with extreme rainfall over South America. Stochastic Environmental Research and Risk Assessment, 38(5), 1769-1782. https://doi.org/10.1007/s00477-023-02653-4

IPCC. (2021). Annex IV: Modes of Variability [Cassou, C., Cherchi, A., & Kosaka, Y. (Eds.)]. In Climate Change 2021: The Physical Science Basis. Contribution of Working Group I to the

Sixth Assessment Report of the IPCC [Masson-Delmotte, V., et al. (Eds.)]. Cambridge University Press, pp. 2153-2192. https://doi.org/10.1017/9781009157896.018

Jones, C. Recent changes in the South America low-level jet. npj Clim Atmos Sci 2, 20 (2019). https://doi.org/10.1038/s41612-019-0077-5

Karoly, D. J. (1989). Southern hemisphere circulation features associated with El Niño-Southern Oscillation events. Journal of Climate, 2(11), 1239-1252. https://doi.org/10.1175/1520-0442(1989)002%3C1239:SHCFAW%3E2.0.CO;2

Keyser, D., & Shapiro, M. A. (1986). A review of the structure and dynamics of upper-level frontal zones. Monthly Weather Review, 114(2), 452-499. https://doi.org/10.1175/1520-0493(1986)114%3C0452:AROTSA%3E2.0.CO;2

Koenker, R., & Bassett, G. (1978). Regression Quantiles. Econometrica, 46(1), 33–50. https://doi.org/10.2307/1913643

Lavell, A., Oppenheimer, M., Diop, C., Hess, J., Lempert, R., Li, J., & Myeong, S. (2012). Managing the risks of extreme events and disasters to advance climate change adaptation. Special report of working groups I and II of the IPCC, 3, 25-64. https://doi.org/10.1017/CBO9781139177245.004

L'Heureux, M.L., Collins, D.C. & Hu, ZZ. Linear trends in sea surface temperature of the tropical Pacific Ocean and implications for the El Niño-Southern Oscillation. Clim Dyn 40, 1223–1236 (2013). https://doi.org/10.1007/s00382-012-1331-2

Lima, A. O., Lyra, G. B., Abreu, M. C., Oliveira-Júnior, J. F., Zeri, M., & Cunha-Zeri, G. (2021). Extreme rainfall events over Rio de Janeiro State, Brazil: Characterization using probability distribution functions and clustering analysis. Atmospheric Research, 247, 105221. https://doi.org/10.1016/j.atmosres.2020.105221

Luo, L., Ke, C. Q., Cai, Y., Li, H., Xiao, Y., Nourani, V., ... & Sankaran, A. (2025). Abrupt decline and subsequent recovery of extreme precipitation associated with Atmospheric Rivers in the Southeastern Tibetan Plateau. Atmospheric Research, 108461. https://doi.org/10.1016/j.atmosres.2025.108461

Maenza, R. A., Agosta, E. A., & Bettolli, M. L. (2017). Climate change and precipitation variability over the western 'Pampas' in Argentina. International Journal of Climatology, 37, 445-463. https://doi.org/10.1002/joc.5014

Maisonnave, T., Hurtado, S.I., Aldeco, L.S. et al. Using climate variability for regional crop yield prediction with machine learning: a case study on sunflower, corn, and wheat in the Argentine pampas. Theor Appl Climatol 157, 21 (2026). https://doi.org/10.1007/s00704-025-05943-9

Marshall, G. J. (2003). Trends in the Southern Annular Mode from observations and reanalyses. Journal of Climate, 16(24), 4134-4143. https://doi.org/10.1175/1520-0442(2003)016<4134:TITSAM>2.0.CO;2

Masiokas, M. H., Villalba, R., Luckman, B. H., Le Quesne, C., & Aravena, J. C. (2006). Snowpack variations in the central Andes of Argentina and Chile, 1951–2005: Large-scale atmospheric influences and implications for water resources in the region. Journal of climate, 19(24), 6334-6352. https://doi.org/10.1175/JCLI3969.1

Medina, F. D., Zossi, B. S., & Elias, A. G. (2025). Changes on the summer Rx1-ENSO and Rx1-SAM relations over Northern Argentina driven by PDO phases. Theoretical and Applied Climatology, 156(2), 95. https://doi.org/10.1007/s00704-024-05350-6

Mo, K.C. and Nogués-Paegle, J. (2001), The Pacific–South American modes and their downstream effects. Int. J. Climatol., 21: 1211-1229. https://doi.org/10.1002/joc.685

Montini, T. L., Jones, C., & Carvalho, L. M. (2019). The South American low-level jet: A new climatology, variability, and changes. Journal of Geophysical Research: Atmospheres, 124(3), 1200-1218. https://doi.org/10.1029/2018JD029634

Nogués-Paegle, J., & Mo, K. C. (1997). Alternating wet and dry conditions over South America during summer. Monthly Weather Review, 125(2), 279-291. https://doi.org/10.1175/1520-0493(1997)125<0279:AWADCO>2.0.CO;2

Olmo, M., Bettolli, M. L., & Rusticucci, M. (2020). Atmospheric circulation influence on temperature and precipitation individual and compound daily extreme events: Spatial variability and trends over southern South America. Weather and Climate Extremes, 29, 100267. https://doi.org/10.1016/j.wace.2020.100267

Olmo, M. E., & Bettolli, M. L. (2021). Extreme daily precipitation in southern South America: statistical characterization and circulation types using observational datasets and regional climate models. Climate Dynamics, 57(3-4), 895-916. https://doi.org/10.1007/s00382-021-05748-2

Pettitt, A.N. (1979), A Non-Parametric Approach to the Change-Point Problem. Journal of the Royal Statistical Society: Series C (Applied Statistics), 28: 126-135. https://doi.org/10.2307/2346729

Reboita MS, Ambrizzi T, Silva BA, Pinheiro RF and da Rocha RP (2019) The South Atlantic Subtropical Anticyclone: Present and Future Climate. Front. Earth Sci. 7:8. doi: 10.3389/feart.2019.00008

Reboita, M. S., da Rocha, R. P., Souza, C. A. D., Baldoni, T. C., Silva, P. L. L. D. S., & Ferreira, G. W. S. (2022). Future projections of extreme precipitation climate indices over South America based on CORDEX-CORE multimodel ensemble. Atmosphere, 13(9), 1463. https://doi.org/10.3390/atmos13091463

Ricetti, L., Hurtado, S. I., Agosta Scarel, E. A., & Cesanelli, A. (2024). Variabilidad del caudal del río Neuquén en las fases de su ciclo anual y su relación con índices climáticos. Meteorologica, 49. https://doi.org/10.24215/1850468Xe026

Ricetti, L., Hurtado, S. I., & Scarel, E. A. (2025a). On the spatio-temporal coherence of extreme precipitation indices in subtropical Argentina. Atmospheric Research, 320, 108082. https://doi.org/10.1016/j.atmosres.2025.108082

Ricetti, L., Hurtado, S. I., Zaninelli, P. G., & Agosta, E. A. (2025b). Determining the percentile threshold of daily extreme precipitation, methods evaluation. Stochastic Environmental Research and Risk Assessment, 39(7), 2887-2902. https://doi.org/10.1007/s00477-025-02998-y

Ricetti, L., Hurtado, S. I., & Agosta, E. A. (2025c). Understanding streamflow variability over drylands in a water-scarce region: a case study in Patagonia. Hydrological Sciences Journal, 70(7), 1157–1175. https://doi.org/10.1080/02626667.2025.2475109

Ricetti, L. (2026). Estudio de índices trimestrales de extremos húmedos de precipitación diaria: Estimación de percentiles, coherencia espacio-temporal, y mecanismos forzantes de su variabilidad de baja frecuencia en noviembre-diciembre-enero y febrero-marzo-abril (Doctoral dissertation, Universidad Nacional de La Plata). https://doi.org/10.35537/10915/197227

Robledo, F. A., Penalba, O. C., & Bettolli, M. L. (2013). Teleconnections between tropical-extratropical oceans and the daily intensity of extreme rainfall over Argentina. International Journal of Climatology. https://doi.org/10.1002/joc.3467

Robledo, F. A., Vera, C., & Penalba, O. C. (2016). Influence of the large-scale climate variability on daily rainfall extremes over Argentina. International Journal of Climatology, 36, 412-423. https://doi.org/10.1002/joc.4359

Ruxton, G. D. (2006). The unequal variance t-test is an underused alternative to Student's t-test and the Mann-Whitney U test. Behavioral Ecology, 17(4), 688-690. https://doi.org/10.1093/beheco/ark016

Santos, M., Fragoso, M., & Santos, J. A. (2017). Regionalization and susceptibility assessment to daily precipitation extremes in mainland Portugal. Applied Geography, 86, 128-138. https://doi.org/10.1016/j.apgeog.2017.06.020

Sardeshmukh, P. D., & Hoskins, B. J. (1988). The generation of global rotational flow by steady idealized tropical divergence. Journal of the Atmospheric Sciences, 45(7), 1228-1251. https://doi.org/10.1175/1520-0469(1988)045<1228:TGOGRF>2.0.CO;2

Sarış, F. (2020). The spatial pattern of selected extreme precipitation indices for Turkey (1975-2012). Bulletin of Geography. Physical Geography Series, (19), 19-30. https://doi.org/10.2478/bgeo-2020-0007

Schär, C., Ban, N., Fischer, E. M., Rajczak, J., Schmidli, J., Frei, C., ... & Zwiers, F. W. (2016). Percentile indices for assessing changes in heavy precipitation events. Climatic Change, 137, 201-216. https://doi.org/10.1007/s10584-016-1669-2

Seager, R., Harnik, N., Kushnir, Y., Robinson, W., & Miller, J. (2003). Mechanisms of hemispherically symmetric climate variability. Journal of Climate, 16(18), 2960-2978. https://doi.org/10.1175/1520-0442(2003)016%3C2960:MOHSCV%3E2.0.CO;2

Seager R., Harnik N., Robinson W.A., Kushnir Y., Ting M., Huang H.P., Velez J. 2005: Mechanisms of ENOSforcing of hemispherically symmetric precipitation variability. Q. J. R. Meteorol. Soc. 131(608): 1501-1527. https://doi.org/10.1256/qj.04.96

Seneviratne, S. I., Zhang, X., Adnan, M., Badi, W., Dereczynski, C., Luca, A. D., ... & Allan, R. (2021). Weather and climate extreme events in a changing climate. https://doi.org/10.1017/9781009157896.013

Simmonds, I., & Lim, E.-P. (2009). Biases in the calculation of Southern Hemisphere mean baroclinic eddy growth rate. Geophysical Research Letters, 36, L01707. https://doi.org/10.1029/2008GL036320

Skansi, M., Brunet, M., Sigró, J., Aguilar, E., Groening, J. A. A., Bentancur, O. J., ... & Jones, P. D. (2013). Warming and wetting signals emerging from analysis of changes in climate extreme indices over South America. Global and Planetary Change, 100, 295-307. https://doi.org/10.1016/j.gloplacha.2012.11.004

Sörensson, A. A., & Ruscica, R. C. (2018). Intercomparison and uncertainty assessment of nine evapotranspiration estimates over South America. Water Resources Research, 54(4), 2891-2908. https://doi.org/10.1002/2017WR021682

Takahashi, K., A. Montecinos, K. Goubanova, and B. Dewitte (2011), ENSO regimes: Reinterpreting the canonical and Modoki El Niño, Geophys. Res. Lett., 38, L10704, doi:10.1029/2011GL047364.

Takaya, K., & Nakamura, H. (2001). A formulation of a phase-independent wave-activity flux for stationary and migratory quasigeostrophic eddies on a zonally varying basic flow. Journal of the Atmospheric Sciences, 58(6), 608-627. https://doi.org/10.1175/1520-0469(2001)058<0608:AFOAPI>2.0.CO;2

Tedeschi, R. G., Grimm, A. M., & Cavalcanti, I. F. (2015). Influence of Central and East ENSO on extreme events of precipitation in South America during austral spring and summer. International Journal of Climatology, 35(8). https://doi.org/10.1002/joc.4106

Thompson, D. W., & Wallace, J. M. (2000). Annular modes in the extratropical circulation. Part I: Month-to-month variability. Journal of Climate, 13(5), 1000-1016. https://doi.org/10.1175/1520-0442(2000)013<1018:AMITEC>2.0.CO;2

Torrence, C., & Compo, G. P. (1998). A practical guide to wavelet analysis. Bulletin of the American Meteorological Society, 79(1), 61-78. https://doi.org/10.1175/1520-0477(1998)079<0061:APGTWA>2.0.CO;2

Torrence, C., & Webster, P. J. (1999). Interdecadal changes in the ENSO–monsoon system. Journal of climate, 12(8), 2679-2690. https://doi.org/10.1175/1520-0442(1999)012<2679:ICITEM>2.0.CO;2

Tuel, A., & Martius, O. (2021). A global perspective on the sub-seasonal clustering of precipitation extremes. Weather and Climate Extremes, 33, 100348. https://doi.org/10.1016/j.wace.2021.100348

Uccellini, L. W., & Johnson, D. R. (1979). The coupling of upper and lower tropospheric jet streaks and implications for the development of severe convective storms. Monthly Weather Review, 107(6), 682-703. https://doi.org/10.1175/1520-0493(1979)107%3C0682:TCOUAL%3E2.0.CO;2

Varuolo-Clarke, A. M., Williams, A. P., Smerdon, J. E., Ting, M., & Bishop, D. A. (2022). Influence of the South American low-level jet on the austral summer precipitation trend in southeastern South America. Geophysical Research Letters, 49, e2021GL096409. https://doi.org/10.1029/2021GL096409

Wang, F., Duan, R. X., Li, Y. F., & Tian, C. R. (2021). Extreme summer precipitation events in China and their changes during 1982-2019. Journal of Environmental Informatics Letters, 6(1), 1-9. https://doi.org/10.3808/jeil.202100066

Wilks, D. S. (2011). Statistical methods in the atmospheric sciences (Vol. 100). Academic Press.

Zhang, X., Alexander, L., Hegerl, G. C., Jones, P., Tank, A. K., Peterson, T. C., ... & Zwiers, F. W. (2011). Indices for monitoring changes in extremes based on daily temperature and precipitation data. Wiley Interdisciplinary Reviews: Climate Change, 2(6), 851-870. https://doi.org/10.1002/wcc.147

Supplementary Files

This is a list of supplementary files associated with this preprint. Click to download.

- Supplementarymaterial.docx